Universidade Federal da Bahia
Instituto de Física

Geometry and Electron Emission Analyses of Random Surfaces

presented by
Caio Porto de Castro

accepted on the recommendation of
Prof. Dr. Thiago Albuquerque de Assis, supervisor
Prof. Dr. Roberto Fernandes Silva Andrade, co-supervisor

A thesis submitted as a partial requirement to be assigned the degree of
DOCTOR OF PHYSICS of Federal University of Bahia
October 2017

Acknowledgements

I would like to thank my supervisor Prof. Dr. Thiago Albuquerque de Assis, Prof. Dr. Caio Mário Castro de Castilho, Prof. Dr. Roberto Fernandes Silva Andrade and Prof. Dr. Hans Jürgen Herrmann. Also, thanks my family and friends. Because all of them, this thesis could became a reality. Finally, thanks to the government funding agencies CAPES, the postgraduate of physics of the UFBA and CNPq.

Dedication

To my parents, Charles and Jesseni.

‘Although each of us is unrepeatable, we are not even exclusive, although we are unique.’

‘Embora cada um de nós seja irrepetível, nós não somos nem exclusivos, embora sejamos únicos.
Mario Sergio Cortella

Abstract

By Fourier transform we generate correlated random surfaces that was used as a tool to study two different fields, statistical physics in terms of the Schramm/Stochastic Loewner Evolution (SLE) and Cold Field Electron Emission (CFE). We have shown that critical exponents of percolating systems are not affected by the form of the distribution of the Fourier coefficient and phase and Fourier phase correlations. Our results of extensive numerical SLE test, indicate that the full perimeters of percolating clusters of correlated surfaces, with negative Hurst exponent, are statistically equivalent, in the scaling limit, to SLE curves. From the perspective of CFE, a more general criterion for detecting and interpreting nonorthodox field emission is proposed and can be applied to any distribution of local field enhancement factors in conducting large-area field emitters (LAFEs). We show that morphology changes on LAFEs can lead to saturation of the Fowler-Nordheim (FN) plot. Finally, we emphasize that the linear behavior of the FN plot does not guarantee that the emission phenomenon is orthodox.

Resumo

Através da transformada de Fourier nós geramos superfícies aleatórias correlacionadas que foram utilizadas para estudarmos dois diferentes campos da Física, Física Estatística no âmbito da evolução de Schramm-Loewner (SLE) e emissão de elétrons por efeito campo elétrico (CFE). Primeiro verificamos que expoentes críticos de sistemas de percolação em surperfícies correlacionadas não apresentaram dependência com as distribuições dos coeficientes e fase de Fourier, bem como devido a correlações na fase. Nossos resultados, após extensivos testes numéricos de SLE, indicaram que o perímetro completo do aglomerado de percolação de sistemas correlacionados, com expoente de Hurst negativo, são estatisticamente equivalentes, no limite de escala, a curvas SLE. Na perspectiva de CFE, propomos um critério mais geral para detectar e interpretar emissões não-ortodoxas, o qual pode ser aplicado para qualquer distribuição de fatores de amplificação em emissores de ampla area de emissão (LAFEs). Mostramos que mudanças morfológicas em LAFEs podem levar à saturação no gráfico de Fowler-Nordheim (FN). Por fim, enfatizamos que um comportamento linear do gráfico de FN não garante que o fenômeno de emissão é ortodoxo.

Contents

List of Tables

List of Figures

Chapter 1

Introduction

Irregular random surfaces are explored in several branches of physics. The sea surface temperature patterns, natural landscapes, 2D turbulence systems, rough thin films, and also possible emitter devices[1–10] can be mapped onto random surfaces characterized by the Hurst exponent, H. This exponent is associated to the height-height spatial correlation between two sites/points on the surface. Given this broad scope, we have analyzed here aspects of the random surfaces according to two distinct frameworks, namely from the point of view of statistical physics and cold field electron emission (CFE).

Similarly to statistical physics models, which can be classified into universality classes based on their critical exponents, two-dimension fractal curves may be classified into universality classes based on their geometrical properties. In this case, a well known of those critical exponents is the fractal dimension of such curves itself. Here, together with other critical exponents, the fractal dimension shows a clear dependence on Hurst exponent. However, the fractal dimension of curves from different physical systems have shown to be equal [5, 6] and, therefore, indicates the need to find a more fundamental property. The important step to clarify this issue was provided by Oded Schramm, who published the theory of Stochastic Loewner ou Schramm-Loewner, Evolution (SLE) [11]. A SLE theory gives insights into the statistical distribution of the curves and, moreover it allows to describe curves belonging to different universality classes by the same process: a one-dimensional Brownian motion. It means that curves statistically

equivalent to the ones generated by expensive computational calculation as random gaussian surfaces[12], optimization process like watershed[13], shortest path[14], or from solving complex partial equation like in turbulence[5, 4], might be simulated with less computational time. The SLE theory was an astounding success, not only rigorously reproducing previously established results, but also answering long standing unsolved problems, like Mandelbrots conjecture for the boundary of a 2D Brownian motion[15]. Also, for the first time, physicists have a rigorous mathematical tool, they can check their predictions in the framework of statistical physics of interfaces. Therefore, in the first part of this thesis, we have used such a powerful description to investigate if such correlated random surfaces may also follow the SLE statistical properties.

The large applicability of random surfaces in modeling physical systems also includes the representation of emitter surfaces. For that, each site/point of the random surface can be a representation of a single emitter. An example of single-tip field emitter is the carbon nanotubes (CNTs). Such arrange of many single emitters configure a large-area field emitter (LAFEs). In many of the cases, each emitter is represented by its local field enhancement factor (FEF) [16], which represents how much the local field is higher, as compared to the external electric field. The FEF is a source of intense research as in the scope of the morphology of the emitter[17-25], as well as extracting from current voltage characteristic curves[26-29].

Cold field electron emission corresponds to a statistical electron-emission regime in which a macroscopic current is emitted when electrons escape from states close in energy to the Fermi level by a Fowler-Nordheim (FN) tunneling. Recently, the interest in developing electron sources, based on CFE, from relatively large substrate areas that support many individual emitters (or sites) has increased [30, 31, 32, 33]. For instance, field emission measurements under typical conditions over large areas (e.g., on a flat panel display) confirmed that CNT's films have good emission properties when an onset macroscopic field of a few $V/\mu m$ was applied[34, 35, 36, 37]. Applications of particular interest are the electron sources in high power microwave vacuum devices [38] or x-ray generators [39]. Examples of reported field emission cathodes for x-ray sources include silicon [40] and CNT emitter arrays[41]. Recently, it has been shown that fluctuations related to statistical distribution of CNT heights may result, with the increasing of the applied voltage, in new luminous spots on the fluorescent screen[42].

However, all those important applications of LAFEs contrast with its not well established theoretical characterization.

We have concentrated ourselves studying LAFEs that show dependence of area emission on the applied field and also a possible degradation process of the emitters. Such considerations were taken into account in order to analyze a more realist physical system. As a consequence, we have proposed a more general criterion for detecting and interpreting these phenomena, since most the explanations for large-area emitters are still extensions from single tip emitters without any correction factor associated to LAFE's characteristics.

This Thesis is organized as follows.

Chapter 2 describes the method used to generate random surfaces, the Fourier filtering method. A quantitative scale analyses of the influence of the different distributions of the Fourier coefficients and phases over the surface generated is discussed. It is presented numerical evidences on the conjectures of the dependence on Hurst exponent of several critical exponents such as the fractal dimension of the percolating clusters and its perimeters, correlation length. We also have verified the consequences of Fourier phases correlation.

In the Chapter 3 we introduce the SLE Theory by explaining conformal invariance, the Riemann mapping theorem, the Loewner equation, Schramm's contributions, and finally describe the numerical SLE test. In sequence, we study isoheight lines extracted from correlated surfaces in the framework of SLE. More precisely, we have accomplished a direct numerical SLE test, as well as a Markovian test for such two-dimensional curves.

Chapter 4 gives an introduction to the Fowler–Nordheim theory, from the Fowler and Nordheim description to the current approach. We present the modern description and notation for the emission current density, including important corrections related to the form of the tunneling barrier and Forbes' contributions.

In the chapter 5 a more general criterion for detecting and interpreting nonorthodox field emission is proposed and can be applied to any distribution of local FEFs in conducting LAFEs. It is also shown a more general theory for extracting the scaled barrier field, f, by considering

the dependence of the formal area of emission of the conducting LAFEs with an applied field.

In Chapter 6 we present a simple model that is able to demonstrate that degradation on the morphology of a conducting LAFE may cause a kinked behavior formed by two clear linear regimes before saturation on the corresponding ordinary FN plot.

The last Chapter 7 presents the final conclusions and remarks.

Chapter 2

Random Surfaces

Many examples of natural systems can be described by random Gaussian surfaces. By analyzing the Fourier expansion of the surfaces much information can be extracted, such that, statistical and morphology properties, from which it is possible to determine the corresponding Hurst exponent and consequently establish the presence of scale invariance. Therefore, in this chapter we study the method we have used to generate random Gaussian surfaces, the Fourier filtering method (FFM), which is built by the Fourier transform. We show that the scale invariance is not affected by the distribution of the modulus of the Fourier coefficients. Furthermore, we investigate the role of the Fourier phases of random surfaces. In particular, we show how the surface is affected by a non-uniform distribution of phases.

This chapter is based on reference [12]:

de Castro, C. P., Luković, M., Andrade, R. F. S. & Herrmann, H. J., *The influence of statistical properties of Fourier coefficients on Random Gaussian surfaces., Scientific Reports*, **7**, 1961 (2017).

2.1 Introduction

Two-dimensional random surfaces can be considered as a generalization of one-dimensional stochastic processes. Often, properties of natural systems, such as sea surface temperatures, rough graphene surfaces and 2D turbulence, can be mapped onto random surfaces [1, 2, 3, 4, 5, 6]. Their scaling properties can be characterized by a single parameter known as the Hurst exponent, H. This exponent is related to the degree of spatial correlation between two points on the surface. For all $H > -1$ the surfaces are long-range correlated, rough and self-affine [6, 44, 45]. Uncorrelated surfaces correspond to an H-value of -1.

Much can be learned about the properties of random surfaces by studying the paths of constant height (lines) extracted from them [44,46-50]. Empirical and numerical studies of these paths suggest that, at the height corresponding to the percolation threshold, they are scale invariant and their fractal dimension depends on the Hurst exponent H [51, 52, 47]. In some cases they also have an additional symmetry, reflected by the conformal invariance of these paths [4, 6]. This means that the statistics of such curves is covariant with respect to local scale transformations [53].

There exist several methods to generate random surfaces [54]. In this work, we consider the Fourier Filtering Method (FFM), where one first creates a random surface in the reciprocal space and then Fourier transform it into real space. Our results are based on high performance calculations, large system sizes as well as tens of thousands of samples.

In the context of random surfaces, it is taken for granted that critical exponents[1], such as the fractal dimension of the percolation cluster and its perimeters, or those related to the correlation length and the susceptibility, depend only on H [55, 56]. In the case of conformal invariance, the current view is not as straightforward. Although conformal theory is not the main topic of this paper, it serves as motivation for our investigations [57, 58, 59, 60, 13]. In particular, it is worth noting that random curves with well defined Hurst exponents do not necessarily exhibit conformal invariance. For example, Bernard *et al.* observed conformal invariance in the

[1]The term 'critical exponent' used in this thesis is in the sense of exponent derivative of power laws dependences.

iso-height lines of vorticity fields of 2D turbulence [4]. They also showed, however, that this property is violated for iso-height lines extracted from surfaces with the same Hurst exponent but with randomly distributed phases of the surface heights in Fourier space. Therefore, it seems that it is not only the Hurst exponent that plays a determinant role in conformal invariance. Furthermore, outside the context of conformal invariance, Kalda, J. shows that gradient-limited surfaces are not characterized only by H[56]. The possible dependence of conformal invariance on phase correlations [4] and the existence of scale-invariant curves with scale-dependent critical exponents [56], has therefore motivated us to investigate whether the scale invariance of iso-height lines of random Gaussian surfaces is also affected in a similar way.

Given that each point of the random surface in reciprocal space is determined by the phase, as well as the magnitude of a complex number, for the sake of completeness we also study the effects of the latter on the scale invariance of the iso-height lines. Therefore, we investigate how the critical exponents, some of them defined by Kodev, J. and Henley, C. L.[52], are influenced by Fourier phases, especially their correlations, as well as the distribution of the magnitudes of the Fourier components.

We show that a non-uniform distribution of Fourier phases introduces symmetries in random surfaces and that a change in the phase correlation length in Fourier space causes a translation of the surface in real space. Furthermore, our results show that changes in the shape of the distribution of Fourier magnitudes, without altering their correlations, have the sole effect of modifying the height magnitudes of the random surfaces. None of the variations described above change significantly the H-dependence of the critical exponents, as conjectured by Schrenk K. J. *et al.* in [47].

2.2 Methods

In this section we present two fundamental methods we have used to generate such random surfaces and find the percolating threshold: the Fourier Filtering Method and the Rank Method, respectively.

2.2.1 Fourier Filtering Method

A set of random real numbers may be interpreted as a surface, where each number corresponds to the height $h(\mathbf{x}) = h(x_1, x_2)$ at coordinates x_1 and x_2 [50, 49, 47, 54, 61]. In order to create correlated random surfaces, we have used the Fourier Filtering Method (FFM)[62, 63, 64, 65, 66, 67], which consists in defining a complex function $\eta(\mathbf{q})$ in Fourier space and then taking the inverse transform to obtain $h(\mathbf{x})$. The complex Fourier coefficients $\eta(\mathbf{q})$ can be written in the form

$$\eta(\mathbf{q}) = \mathsf{c}(\mathbf{q}) \exp(2\pi\phi(\mathbf{q})), \tag{2.1}$$

where $\mathbf{q} = (q_1, q_2)$ is the frequency in Fourier space, $\mathsf{c}(\mathbf{q})$ the magnitude and $\phi(\mathbf{q})$ the phase. In order to obtain a random surface with the desired properties, we choose the power spectrum $S(\mathbf{q})$ of the surface in the form of a power law such that

$$S(\mathbf{q}) \sim |\mathbf{q}|^{-\beta_c} = \left(\sqrt{q_1^2 + q_2^2}\right)^{-\beta_c} \tag{2.2}$$

where $\beta_c = 2(H + 1)$ [54] defines the Hurst exponent. Then, we apply the power-law filter to a real random variable $u(\mathbf{q})$ obtaining for the magnitude

$$\mathsf{c}(\mathbf{q}) = [S(\mathbf{q})]^{1/2} u(\mathbf{q}). \tag{2.3}$$

In general, $u(\mathbf{q})$ is Gaussian distributed with finite variance, $\phi(\mathbf{q}) \in [0, 1]$ is a uniformly distributed noise and $\mathsf{c}(\mathbf{q})$ must satisfy the conjugate symmetry condition, $\mathsf{c}(\text{-}\mathbf{q}) = \overline{\mathsf{c}(\mathbf{q})}$ [54]. Without loss of generality, we will consider the case where $u(\mathbf{q})$ has unit variance.

The choice of the power spectrum as a filter is justified by the Wiener-Khintchine theorem [54, 68], which states that the autocorrelation function, $C(\mathbf{r})$, of a time series is the Fourier transform of its power spectrum. Therefore, from the inverse discrete Fourier transform of $\eta(\mathbf{q})$ we obtain $h(x_1, x_2)$

$$h(x_1, x_2) = \sum_{q_1=0}^{N-1} \sum_{q_2=0}^{N-1} \eta_(q_1 q_2) \exp(-2i\pi(q_1 x_1 + q_2 x_2)) \tag{2.4}$$

with the desired power-law correlation function [54, 47, 44]

$$C(\mathbf{r}) \sim \mathbf{r}^{2H}. \tag{2.5}$$

According to the definition above, if $H = -1$ and therefore $\beta_c = 0$, the power spectrum in Eq. 2.2 becomes independent of the frequency, giving rise to uncorrelated surfaces. As H increases from -1, height-height correlations are introduced into the surface.

For any random surface defined on a lattice with $H \geq -1$, the percolation threshold p_c can be determined using the well established *rank method*. Moreover, a conjecture was recently put forward for the H-dependence of the fractal dimension and critical exponents at the corresponding critical point p_c [47]. It should also be noted that, as a consequence of the extended Harris criterion [55, 69, 48, 70, 71, 72], there are going to be some critical exponents of 2D systems that are not influenced by correlation effects related to $H \in [-1, -3/4]$, implying that, for those Hurst values, the exponents are expected to be the same as for the uncorrelated system [47].

In the case of self-affine surfaces, for which $H > 0$, the percolation threshold is not well defined, since there is no unique value of the surface height at which the system percolates. Nevertheless, in this case also, it is possible to extend some concepts of percolation theory and relate them to H [44, 45].

2.2.2 Rank Method

After generating the discrete random Gaussian surfaces, we use the rank method[73] to reach the percolation threshold in the following way. One first ranks all sites in the landscapes according to their height, from the smallest to the largest value. Then, a ranked surface is constructed where each site has a number corresponding to its position in the rank, so that the following percolation model can then be defined. Initially, all sites of the ranked surface are unoccupied. Then the sites are occupied one by one, according to the ranking. At each step, the fraction of occupied sites p increases by the inverse of the total number of sites on the surface, thereby changing the configuration of occupied sites. By continuing this procedure a critical height h_c is reached at which the occupied neighboring sites create a spanning cluster (percolation cluster) that connects two opposite borders of the surface (fig. 2.1).

2.3 Clusters and perimeters

At the critical height, the fraction of occupied sites reaches the percolation threshold p_c. From the percolation cluster we extracted the fractal iso-height lines that correspond to the *complete perimeter* and *accessible perimeters* [47, 44, 74, 75]. The complete perimeter consists of all bonds between the percolating cluster and unoccupied sites. This is illustrated in fig. 2.1, where light-gray represents the percolating cluster and the black line follows the complete perimeter.

The accessible perimeter is obtained by eliminating from the complete perimeter all line segments within fjords with a bottleneck equal to the length r of the current stick. This procedure stems from the yardstick method used to measure the perimeter's fractal dimension. Here, for each value of r, the length of any curve is defined by the number of straight yardsticks N_r required to go from one extreme to the other by jumping from one point on the curve to the next at a distance r. Then, the fractal dimension df_p is defined by

$$N_r \sim r^{-df_p}. \tag{2.6}$$

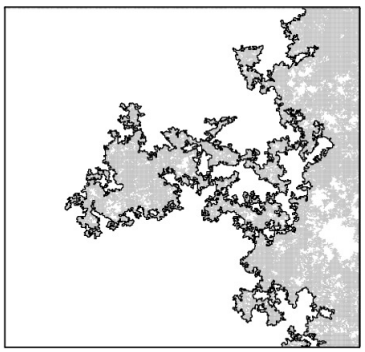

Figure 2.1: Schematic picture of the percolating cluster (light gray) connecting the top of the square with the bottom. The white region corresponds to sites that do not belong to the percolating cluster (unoccupied sites and other clusters) and the black line is the external (complete) perimeter. This map was generated by OriginPro 2016 (64-bit) Sr1 b9.3.1.273 (http://www.originlab.com/).

Fig. 2.2.a shows an arbitrary curve where the black dot, in the center of the green circle, indicates the current stick position. During this specific search for the next point on the curve, three possible positions indicated by red, green and blue X's are found. If the option to always take the closest position along the curve (red X) is made, the complete perimeter is obtained. On the other hand, if one always takes the most distant point along the curve (blue dot), which does not avoid the external border, the accessible perimeter is obtained. Indeed, this rule skips points inside fjords and accesses only the external boundary of the coast, independently of the chosen direction (in the case of Fig. 2.2 either bottom-up or top-down), because there is no preferential correlation direction. Fig. 2.2.b shows the difference between the considered paths for one particular stick size.

2.4 Results and Discussion

Having described the method for generating random surfaces using two sets of random variables, $u(\mathbf{q})$ and $\phi(\mathbf{q})$, we now discuss how a surface is affected by changing the form of their respective distributions.

Although common [54], it is not always the case that $u(\mathbf{q})$ follows a Gaussian distribution and $\phi(\mathbf{q})$ a uniform one. For example, Giordanelli *et al.* [6] found that for graphene sheets $u(\mathbf{q})$ is well fitted by $f(|u|) \propto c_1|u|\exp^{-c_2|u|^2}$, where c_1, c_2 are parameters of the fit. They

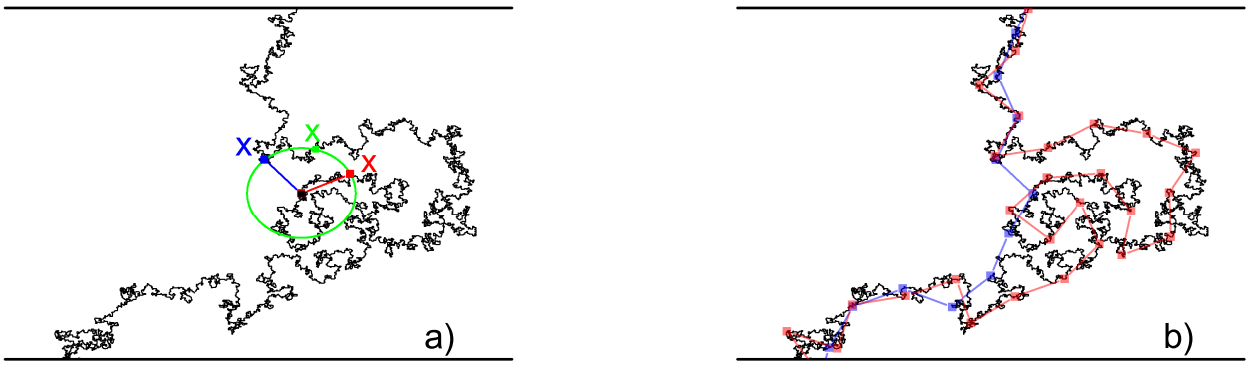

Figure 2.2: a) Illustration of the rules used to compute the fractal dimension of the complete and accessible perimeters with the yardstick method. Suppose the sticks start to follow the coast from the bottom. The green circle shows the region of coast accessible to a particular stick. The **X**'s represent the next possible starting points of that particular stick. If the closest point along the coast (red **X**) is always chosen as the next starting point, we obtain the complete perimeter. If, on the other hand, the most distant point (blue **X**) is chosen, then we obtain the accessible perimeter. Here, points such as the green X, which are neither the closest nor the most distant from the center of the circle, are disregarded. b) Paths made by sticks of equal sizes of the complete (blue sticks) and accessible (red sticks) perimeters.

also found that the Fourier phase distribution $\phi(\mathbf{q})$ is bi-modal rather them uniform [6], as illustrated in Fig. 2.3. On the other hand, for the vorticity field of 2D turbulence, we found through independent analysis that $u(\mathbf{q})$ follows a Gaussian distribution and that $\phi(\mathbf{q})$ is nearly uniformly distributed used. Both $u(\mathbf{q})$ and $\phi(\mathbf{q})$ are obtained by creating a histogram of the random terms of the Fourier transform of the surface being studied.

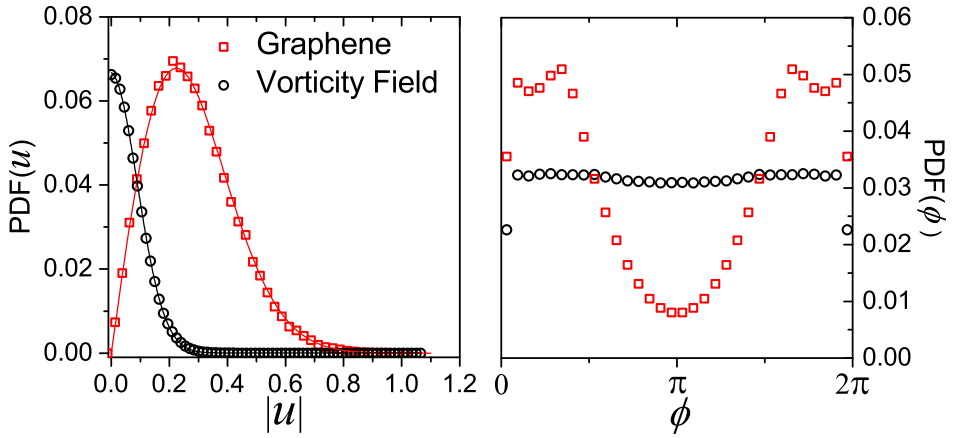

Figure 2.3: Probability density function of $|u(\mathbf{q})|$ (left) and $\phi(\mathbf{q})$ (right) in the case of the graphene sheet (red squares) and the vorticity field (black circles). The red and black curves in left panel are best fits for $f(|u|) \propto c_1|u| \exp^{-c_2|u|^2}$ and the Gaussian function, respectively.

By an adequate choice of the u(q) and $\phi(q)$ distributions, we were able to generate FFM surfaces

that are statistically similar to those in graphene and the vorticity fields in 2D turbulence. This allowed us to investigate how different distributions influence the resulting random surfaces.

Fourier phases

We start by showing the results obtained for three different $\phi(\mathbf{q})$ distributions (Gaussian, uniform and bimodal), while always keeping the same Gaussian distributed $u(\mathbf{q})$. Applying the method described in the previous section, we obtained the dependence of the fractal dimension of the complete ($d^{com}_{f,H}$) and accessible ($d^{acc}_{f,H}$) perimeters on H, as illustrated in fig. 2.4. Since exact values for the fractal dimension of those perimeters are known only for $H = -1$ and $H = 0$, all other proposed analytical dependencies on H are conjectures supported by numerical results [47, 98, 99, 100]. In the case of uncorrelated surfaces, $d^{com}_{f,H=-1} = 7/4$ and $d^{acc}_{f,H=-1} = 13/10$. When H increases from -1, the fractal dimension of complete and accessible perimeters start to converge. Once the surfaces are described by a discrete Gaussian Free Field [101] for $H = 0$, the results consistently indicates $df^{com}_{H=0} = df^{acc}_{H=0} = 3/2$. Our results therefore point towards the absence of any dependence of df^{com}_{H} and df^{acc}_{H} on the shape of the distribution of $\phi(\mathbf{q})$. As shown in fig. 2.4, the H-dependence of df^{com}_{H} and df^{acc}_{H} agrees with the conjectures by Schrenk K. J. [47] for both, long-range correlated (fig. 2.4.a) and rough surfaces (fig. 2.4.b).

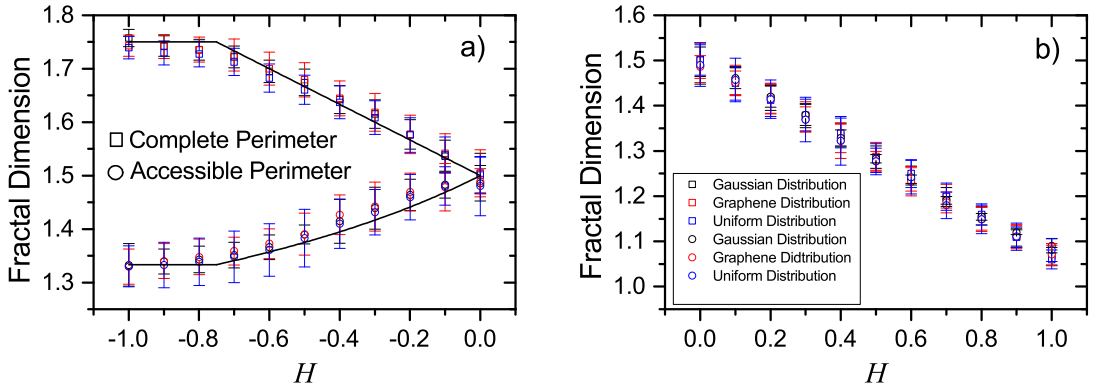

Figure 2.4: Fractal dimension of the complete and accessible perimeters as a function of H, for a) $H < 0$ and b) $H > 0$, and different $\phi(\mathbf{q})$ distributions. In a), the black lines are conjectures proposed by Schrenk K. J. *et al.* [47]. All values are averages over at least 10^4 samples and error bars are defined by the variance of the distribution.

At first glance, the influence of the Fourier phases on the random surface might not be obvious.

However, we notice that the phase distribution mainly influences inversion symmetries with respect to the center of the surface, as shown in fig. 2.5. In order to introduce this effect, $\phi(\mathbf{q})$ is given by a Gaussian distribution with a very small variance, i.e. a peaked distribution . In fig. 2.5 it is possible to identify the same morphological structures when the figure is rotated by an angle π. This occurs because, as the variance goes to zero, the distribution values of the Fourier phases converge to a constant (the mean value) accentuating the symmetry effect[102]. In the limiting case of zero variance the distribution collapses onto a constant value, producing a perfect inversion symmetry in real space. Therefore, in order to avoid this symmetry effect a uniform distribution is used.

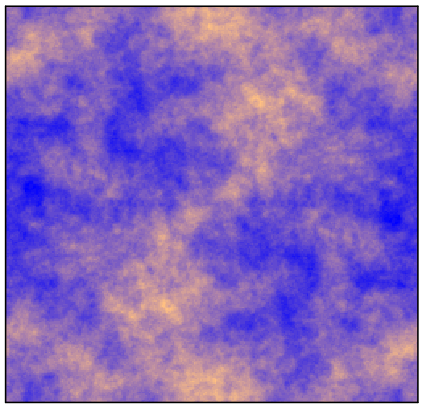

Figure 2.5: Surface map with inversion symmetry with respect to the center. This symmetry of the surface results from the use of a Gaussian distribution $\phi(\mathbf{q})$ with a small variance $\sigma = 0.001$.

Correlated phases

It turns out that the Fourier phases from the vorticity fields and graphene sheets that we analyzed are uncorrelated[6]. Nevertheless, in order to understand how correlations affect random surfaces, we generated some samples with artificially correlated Fourier phases. For this purpose, we introduced correlations in the Fourier phases by applying the FFM twice. First we used the FFM to create a surface of correlated random phases in $\mathbf{q}$-space with Hurst exponent H_φ, according to the Eq. 2.1. Applying the FFM again, we generate Gaussian surfaces with Hurst exponent H and with the desired coefficients and correlated Fourier phases. Using always the same distributions of $\phi(\mathbf{q})$ and $u(\mathbf{q})$ and keeping fixed the value of H and the seed of the random number generator, we studied the changes in the surface caused by a change in

H_φ. We found that the correlation of Fourier phases causes a linear translation of the random surfaces (fig. 2.6). A change in H_φ modifies the slope of the power spectrum (Eq. 2.2), causing all sites of $\phi(\mathbf{q})$ to shift proportionally, which means that a constant value is added to the Fourier phases, causing a translation on the random surface (in real space)[102].

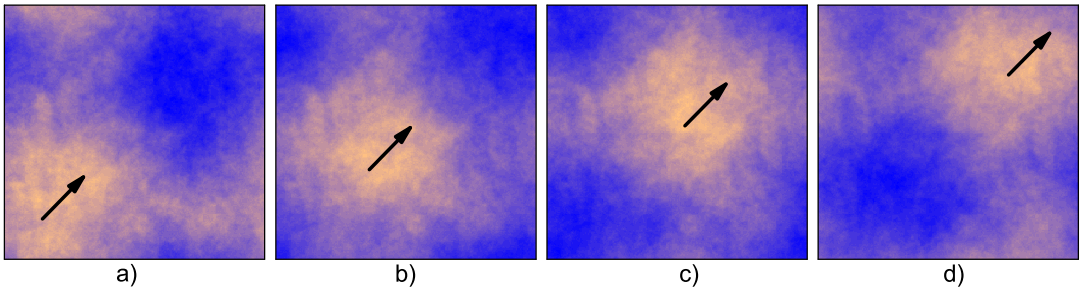

Figure 2.6: Maps of phase correlated surfaces. Panels a), b), c), and d) show examples of surfaces with $H = 0.5$ and $H_{phase} = -0.9, -0.2, 0.1$, and 0.4 respectively. The arrows serve as a guide to show the linear translation of the random surface due to correlations introduced between the Fourier phases.

Magnitude of the Fourier coefficients

We generated sets of random surfaces, each having $\phi(\mathbf{q})$ uniformly distributed but with a different distribution of $u(\mathbf{q})$: Gaussian, uniform and the distribution found by Giordanelli *et al.* in graphene. We then determined the average values of two critical exponents of percolation corresponding to each set of surfaces with a different u-distributions. We first considered the H-dependence of the correlation length critical exponent ν_H for $-1 \leq H \leq 0$. It is well established that the critical point $p_c \simeq 0.592746$ [55, 50, 48, 71] is the infinite system size limit of the percolation threshold $p_c(H, L)$, which is H-dependent for finite system sizes, L. Furthermore, the expected scaling behavior [74, 75, 47] is

$$|p_c(H, L) - p_c| \sim L^{-1/\nu_H}, \tag{2.7}$$

with $\nu_H = -1/H$ [47, 103, 104]. Our numerical results in fig. 2.7 not only confirm that the scaling relation in Eq. 2.7 is respected no matter which one of the three u-distributions we use but also that the value of p_c remains unchanged.

A consequence of the scaling relation in Eq. 2.7 is that in the asymptotic limit it is sufficient to compute the critical exponents at the percolation threshold, p_c.

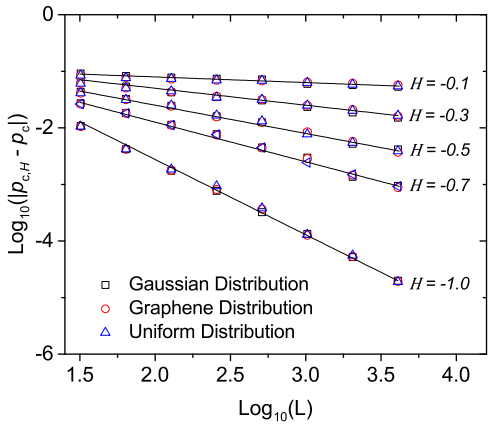

Figure 2.7: Scale analysis of the convergence of the percolation threshold $p_{c,H}$. For the square lattice, the site percolation threshold p_c for uncorrelated surfaces is $p_c \simeq 0.592746$. The black lines serve as guides to the eye with slope $H = -1/\nu_H$ [74, 75, 47].

At this critical point, the percolation cluster is a fractal with fractal dimension d_f. The occupancy, M_{max}, which is the number of sites that belong to the percolation cluster, scales with lattice size L as,

$$M_{max} \sim L^{d_f}. \tag{2.8}$$

Using Eq. 2.8 we recovered numerically the value of the fractal dimension as a function of the Hurst exponent. In fig. 2.8 our results show that the value of the fractal dimension of the percolation cluster remains the same for all three distributions of $u(\mathbf{q})$.

We also checked the H-dependence of the susceptibility critical exponent γ by considering the scaling behavior of m_2, the second moment of the distribution of the cluster sizes at p_c defined as [55]

$$m_2 = \sum_k \frac{M_k^2}{N} - \frac{M_{max}^2}{N}. \tag{2.9}$$

Here, the sum runs over all clusters, where M_k is the mass of cluster k, and we use the fact that the following scaling behavior holds [55]:

$$m_2 \sim L^{\gamma_H/\nu_H}. \tag{2.10}$$

For uncorrelated percolation ($H = -1$), $\gamma_{H=-1} = 43/18$, $\nu_{H=-1} = 4/3$, so that $d_f = 91/48$ and $\gamma_{H=-1}/\nu_{H=-1} = 43/24$ [55]. Fig. 2.8 shows the dependence on $H \in [-1, 0]$ of both critical exponents, the fractal dimension of the percolation cluster and the exponent ratio γ/ν, for different distributions of $u(\mathbf{q})$.

In conclusion, our results suggest that both exponents, d_f and γ/ν, are independent of the distribution of $u(\mathbf{q})$.

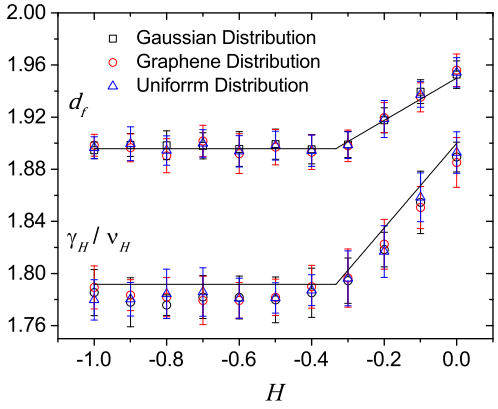

Figure 2.8: Fractal dimension d_f of the percolation cluster and critical exponent ratio γ_H/ν_H as a function of the Hurst exponent H for surfaces with different distributions of $u(\mathbf{q})$. The black lines are conjectures proposed by Schrenk K. J. *et al.* [47] based on the hyperscaling relation [55]. All values are averages over at least 10^4 realizations and error bars are defined as the variance of the distribution of their values.

2.5 Conclusions

We considered two concrete examples of random surfaces, namely, the vorticity field of turbulent systems in two dimensions and rough graphene sheets. We investigated how these random surfaces and in particular the critical exponents are influenced by the presence of phase correlations and by changes in the distribution of the Fourier coefficient magnitudes and Fourier phases. Our results show that the Fourier phases distribution of the vorticity field and graphene sheets, within error bars, lead to the same value for the fractal dimension of the complete and accessible perimeters. We also showed that long-range phase correlations in Fourier space lead to a translation of the random surfaces, and that they do not have any influence on their statistical properties. For different distributions of magnitude of Fourier coefficients our results

suggest there is no H dependence of the fractal dimension of the percolation cluster and susceptibility exponent. In addition, we recovered for the critical exponents the same H-dependence as conjectured by Schrenk K. J. [47]. Although we have only considered three examples of Fourier coefficient distributions, we do not expect different results for any other distribution with finite variance.

Chapter 3

Schramm-Loewner Evolution Theory

In this chapter, we present some aspects of the SLE theory. The original papers on SLE are long and difficult, using, moreover, concept and methods foreign to most physicists. We suggest the references [80, 81, 82, 83, 84] for the proofs we will skip.

One of the most exciting concepts in theoretical physics are those that relate algebraic properties to geometrical ones. As examples of this we can cite the patterns of the paths of Brownian motion, the forms of percolating clusters, the shapes of snowflakes and phase boundaries, or still the geometric meaning of the equations of general relativity, and their realization in the shapes of possible universes and in black holes.

In 1920 Loewner[76] shown that any such non-crossing curve, in the plane, can be described by a dynamical process called Loewner evolution, in which the curve is imagined to be grown in a continuous fashion. Loewner considered the evolution of the analytic functions which conformally maps the region outside the curve into a standard domain. This evolution, and therefore the curve itself, turns out to be completely determined by a real continuous function, $\zeta(t)$. For random curves, $\zeta(t)$ is also random. The seminal contribution of Schramm[11] affirms that if the measure on the curve is comformally invariant, the only possibility is that $\zeta(t)$ be a one-dimensional Brownian motion, characterized only by a single parameter, namely the diffusion constant κ. It should apply to any critical statistical mechanics model in which it is possible to extract this non-crossing path on the lattice, as long as their continuum limits obey the

underlying conformal invariance property. Especially, for the 2D percolation model, Smirnov [77] shows the conformal invariance property for the continuum limit of site percolation and, together with Werner[78], present a rigorous derivation of the values of the critical exponent.

Two classes of SLE have been defined[11]: the radial and the chordal SLE. They differ by the positions of the end points connected by the random sets. The radial SLE related to curves, joining usually 0 to 1 in the open unit disk U, while the chordal SLE, related to curves started at the origin to the point at infinity in the upper half-plane, $\mathbb{H} = \{z, Im(z) > 0\}$. Below, we shall only consider the so-called chordal SLE.

3.1 Conformal Mappings

Since the 1980s, starting from the work of Belavin, Polyakov and Zamolodchikov and of Cardy, the extreme usefulness of conformal invariance in understanding 2D critical phenomena has been realised[79].

A conformal map or a bijective holomorphic function[1] $f(z)$, of a simple connected domain $\mathbb{D} \neq \mathbb{C}$ onto another simply connected domain $\mathbb{D}' \neq \mathbb{C}$, is a one-to-one map which preserves angles. It is called simply connected domain if it contains no holes. That is, if γ_0 and γ_1 are two curves in $\mathbb{D}$, which intersect each other at a certain angle, then their images $g \circ \gamma_0$ and $g \circ \gamma_1$ must intersect at the same angle. In practice this means that a conformal map $g : \mathbb{D} \to \mathbb{D}'$ is a bijective and analytic function on $\mathbb{D}$, and therefore has nonzero derivative everywhere on $\mathbb{D}$ and the inverse g^{-1} is also conformal. More precisely, a domain is simply connected if its complement in the complex plane is connected or, equivalently, if every closed curve in the domain can be contracted continuously to a single point of the domain. The main theorem behind the conformal maps is the Riemann mapping theorem that we will be discussed in the next section.

[1] A holomorphic function is a complex-valued function that is complex and differentiable in a neighborhood of every point in its domain of definition.

3.2 The Riemann Mapping Theorem

The Riemann mapping theorem states that two any simply connected proper subset of the complex plane can be conformally mapped onto another. Then, there exist a unique conformal map $g : \mathbb{D} \to \mathbb{D}'$ such that $g(0) = z$, $g'(0) > 0$.

When the domain $\mathbb{D}$ differs only locally from the upper half plane $\mathbb{H}$, that is, if $\mathbb{K} = \mathbb{H} \setminus \mathbb{D}$ it is bounded. Such a set $\mathbb{K}$ is called a hull. As we are interested in 2D curves, the hull is basically a compact set bordering the path. Such definition guarantee that the hull $\mathbb{K}$ is always simply connected because, when the path touches itself, all the space trapped inside the loops formed belong to the hull. Then, for any hull $\mathbb{K}$, there exists a unique conformal map, denoted by g_K,

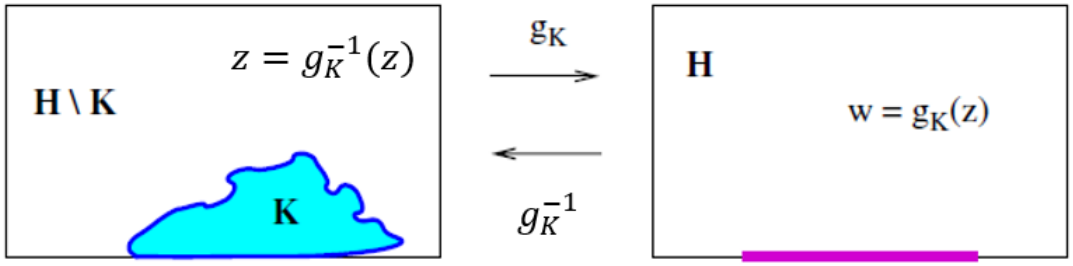

Figure 3.1: An example of hull K in the upper hall plane together and the conformal map $g_K^{-1} : \mathbb{H} \to \mathbb{H} \setminus \mathbb{K}$ and its inverse $g_K : \mathbb{H} \setminus \mathbb{K} \to \mathbb{H}$[82] .

that maps the boundary of one region onto the boundary of the other, i.e., sends $\mathbb{H} \setminus \mathbb{K}$ onto $\mathbb{H}$, such that satisfies the normalization condition,

$$\lim_{|z|\to\infty} g_K(z) - z = 0 \tag{3.1}$$

known as hydrodynamic normalization. The uniqueness of the conformal map results from the condition that $g_K(z) \sim z$ for $|z| \to \infty$. So, the conformal map g_K can be chosen to map infinity to infinity, as,

$$g_K(z) = bz + a_0 + \frac{a_1}{z} + \frac{a_2}{z^2} + ... \quad . \tag{3.2}$$

By Eq. 3.1 we have $b = 1$ and $a_0 = 0$ and, therefore, around infinity g_K have the form,

$$g_K(z) = z + \frac{a_K}{z} + O(|z|^{-2}) \quad , \tag{3.3}$$

where a_K is a real function called half-plane capacity. The form of a_K is not straightforward deduced which has demanded some effort from mathematicians. Based on parametrization of the trace, a_K, a priori, may have several forms as long as it obeys some properties like positivity, continuity and monotonicity[85, 86]. We adopt a common parametrization, $a_K = 2t$.

3.3 Loewner Differential Equation

Loewner's idea [76] was to describe a path $\gamma(t)$, defined by a real parameter t, and the evolution of the tips τ_t in terms of the evolution of the conformal mappping $g_t(z)$. Such conformal mappings are based on the Reimann mapping theorem which guarantees the existence of a conformal transformation that maps any two regions of the complex plane into one another, as described in the sections 3.1 and 3.2. The connection between the path and the conformal mappings is made by a continuous real function $\zeta(t) = g_t(\gamma_t)$ named driving function. Once $\gamma(t)$ is part of the boundary $\mathbb{H} \setminus \gamma_{[0,t]}$ (hull) one is able to map it to a point in the border of the domain $\mathbb{H}$ by $\zeta(t)$.

Lets consider that $\gamma(t)$, with $t \geq 0$, is a continuous non-crossing path in a upper half complex plan $\mathbb{H}$ which starts at the origin, as exemplified in Fig.3.2. Then, based on all assumptions

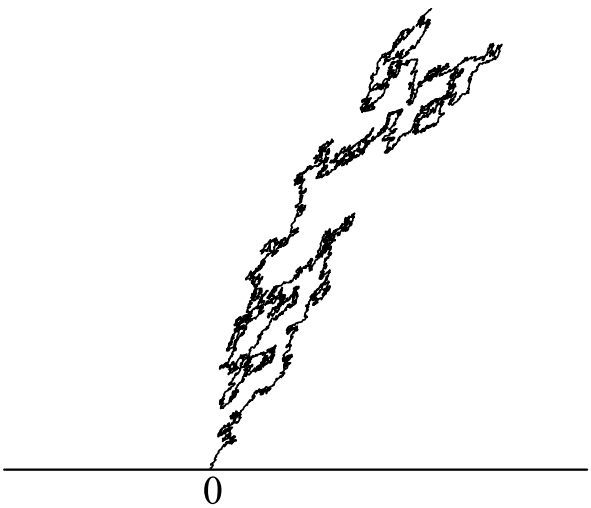

Figure 3.2: An example of chordal trace in a upper half plane $\mathbb{H} = \{z : Im\{z\} \geq 0\}$ with $\gamma_0 = 0$ and $\gamma_\infty = \infty$.

already made related to the conformal map, the Reimann mapping theorem, for all $z \in \mathbb{H}$, the

conformal maps $g_t(z)$, expressed by Eq. 3.3, with the parametrization $a_K = 2t$, satisfies the Loewner differential equation

$$\frac{dg_t(z)}{dt} = \frac{2}{g_t(z) - \zeta(t)} \quad , \quad g_0(z) = z, \tag{3.4}$$

driven by a suitably defined continuous function $\zeta(t)$ (driving function), as illustrated in Fig.3.3. So, from a path $\gamma(t)$ one has $g_t(z)$ and, finally may compute $\zeta(t)$ by solving the Loewner

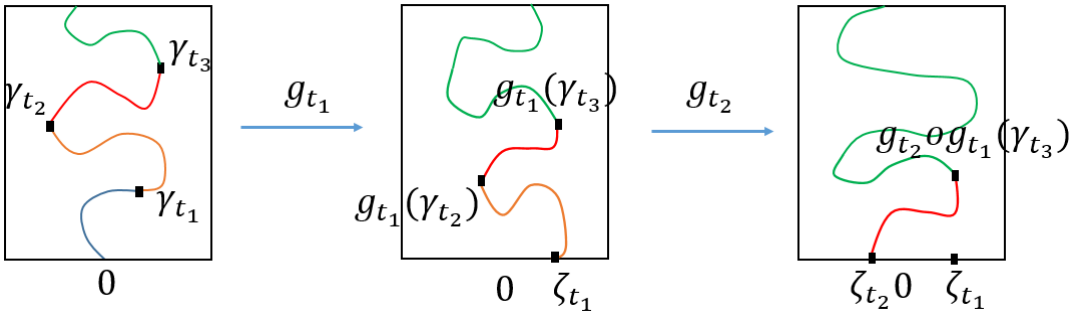

Figure 3.3: Scheme of the evolution of the Loewner equation. For each time step there is a conformal map g_t that maps the upper half plane minus the hull $\mathbb{K}_t$, related to the path γ_t, to the upper half plane itself, $g_t : \mathbb{H} \setminus \gamma_{[0,t]} \to \mathbb{H}$. The point on the boundary of $\mathbb{H}$ where the trace is mapped is the driving function ζ_t.

differential equation. But also the other way around is possible, starting from a suitable $\zeta(t)$ from which one extracts the curve by taking the limit,

$$\gamma_t = \lim_{z \to 0} g_t^{-1}\left(\zeta(t) + z\right), \tag{3.5}$$

In our analyzes, we start from a path and, by solving the Loewner equation, we investigate the statistical properties ζ_t. For a more rigorous mathematics definitions one can follow [76, 85, 86].

3.4 Schramm-Loewner Evolution

It was conjectured in [88], about thirty years ago, that in the continuous limit of the interfaces of 2d statistical systems at criticality should be conformally invariant (in an appropriate sense). This statement was made really precise and powerful by Oded Schramm[11], who understood

what are the consequences of a conformal invariance for a set of random curves and how to exploit them. This led him to the definition of the Schramm Loewner evolution (SLE) theory. The new description focuses directly on non-local structures that characterize a given system, be it a boundary of an Ising or percolation cluster, or loops in the O(n) model, as examples. This description uses the fact that all these non-local objects (path) become random curves at a critical point in the continuum limit, and these curves may be precisely characterized by the stochastic dynamics. It was Schramm's idea that one can use Loewner equation to describe conformally invariant random curves. If one chooses $\zeta(t)$ to be a random real function that satisfies certain conditions: (i) if $\zeta(t)$ is continuous with probability one, (ii) have independent identically distributed increments and (iii) if $\zeta(t)$ is reflection invariant ($x + iy \to -x + iy$). Then, if such $\zeta(t)$ follows these three conditions, it can only be a scaled version of the Brownian motion obeying the familiar Langevin equations,

$$\left\langle (\zeta(t) - \zeta(t'))^2 \right\rangle = \kappa |t - t'| \tag{3.6}$$

where κ is a dimensionless constant, diffusion coefficient, whose value is a very important determinant of the statistical properties of the curve. Once $\zeta(t) = \sqrt{\kappa} B_t$, with $\kappa \geq 0$ and $(B_t)_{t \geq 0}$ a one-dimensional standard Brownian motion, then by Eq.3.4 one can generate SLE_κ with different properties[95]. Note that we may also think in a opposite way. From a such path, by solving the Loewner equation one extracts the driving function ζ_t and, therefore, if ζ_t is a one-dimension Brownian motion, in the continuum limit, the path are SLE with a specific κ. Up to here, we refer to SLE at a particular value of κ as SLE_κ, as usual.

Higher values of κ means a more sinuous Brownian motion, implying in a more sinuous generated trace. For $0 < \kappa \leq 4$ the trace is not sinuous enough to touch itself. When $4 < \kappa < 8$ the trace become sinuous enough to touch itself where, as soon as κ gets close to 8, the hull eventually swallow all domain. Finally, if $\kappa \geq 8$ the trace spacing filling the domain. An example of this SLE phases is shown in Fig.3.4.

The sinuosity of the trace can be associated to its fractal dimension, d_f, with its dependence

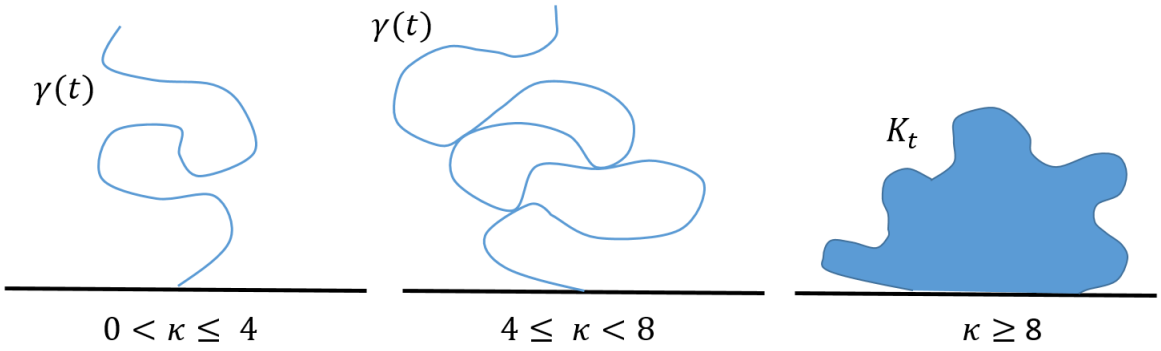

Figure 3.4: Illustrative examples of the SLE phases.

on κ proved by Beffara [96] as being,

$$d_f = min\left(1 + \frac{\kappa}{8}, 2\right). \tag{3.7}$$

Schramm have observed that, by satisfying these previous conditions for $\zeta(t)$ and solving the Loewner equation, one is able to generate conformally invariant traces as consequence of two crucial properties: the domain Markov property and the stationarity of increments of such conformally invariant interfaces. The Markov and stationarity of increments property make it plain that to understand the distribution of the full interface it is enough to understand the distribution of a small, or even infinitesimal, initial segment, and then 'glue' segments via conformal maps.

To describe the domain Markov property and the conformal invariance of such trace γ, lets define a measure $\mu(\gamma; \mathbb{D}, r_i, r_j)$ in a domain $\mathbb{D}$ of such trace γ that connects two points on the boundary $\delta\mathbb{D}$ of $\mathbb{D}$. The domain Markov property guarantee that if γ is divided into two disjoint parts: $\gamma_{3,1}$ from r_3 to r_1, and $\gamma_{3,2}$ from r_3 to r_2. The conditional measure $\mu(\gamma_{3,1}|\gamma_{3,2}; \mathbb{D}, r_1, r_2) = \mu(\gamma_{3,1}; \mathbb{D} \setminus \gamma_{3,2}, r_3, r_1)$, that is, the measure is statically equivalent in both domains. This means that with $\gamma_{3,1}$ and $\gamma_{3,2}$ starting in the same point r_3, the conditional measure of the trace $\gamma_{3,1}$ that have $\gamma_{3,2}$ in the domain $\mathbb{D}$ (box a in Fig.3.5) is the same that the measure in the domain $\mathbb{D}$ minus $\gamma_{3,2}$, $\mathbb{D} \setminus \gamma_{3,2}$ (box b in Fig.3.5).

Now, let f be a conformal mapping of the domain $\mathbb{D}$ onto of $\mathbb{D}'$, so that the points (r_i, r_j) on

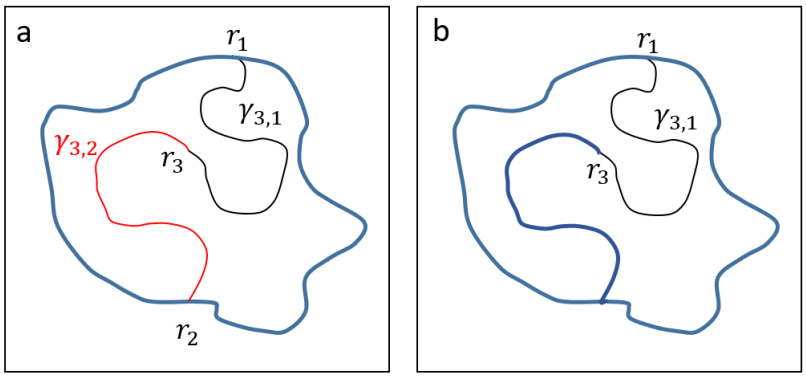

Figure 3.5: (a) The conditional measure of $\gamma_{3,1}$ with $\gamma_{3,2}$ in the domain $\mathbb{D}$ ($\mu(\gamma_{3,1}|\gamma_{3,2};\mathbb{D},r_1,r_2)$) is statically equivalent to (b) the measure of $\gamma_{3,1}$ in a domain $\mathbb{D}$ with $\gamma_{3,2}$ removed ($\mu(\gamma_{3,1};\mathbb{D}\setminus\gamma_{3,2},r_3,r_1)$), that is, $\mathbb{D}\setminus\gamma_{3,2}$.

the boundary $\delta\mathbb{D}$ are mapped to points $(r_i^{'},r_j^{'})$ on the boundary $\delta\mathbb{D}'$. The measure μ on traces in $\mathbb{D}$ induces a measure $f*\mu$ on the image traces in $\mathbb{D}'$. The conformal invariance property states that this is the same as the measure which would be obtained as the continuum limit of lattice traces from $(r_i^{'},r_j^{'})$ in $\mathbb{D}'$. That is

$$(f*\mu)(\gamma;\mathbb{D},r_i,r_j)=\mu(f(\gamma);\mathbb{D}',r_i^{'},r_j^{'}). \tag{3.8}$$

In practice, for example, the conformal invariance guarantee that, in the continuum limit, a trace generated in a square domain is statistically equivalent to one conformally transformed to a circular domain.

3.5 Numerical Method

As mentioned before, the SLE approach may be used for two different analyses: starting from a one dimension Brownian motion with specific κ generates random conformal invariant curves which also obey the Markov properties and from such candidate SLE curve extract the driving function to investigate if its is a one dimension Brownian motion. We took the second option in order to verify if the border of percolation clusters from correlated random surfaces may be SLE_k curves. However, we will start the description of the algorithm assuming we have a one-dimension Brownian motion ζ_t and, by solving the Loewner's equation, extract the

correspondent curve. In this section we describe the well establish algorithm used throughout this thesis, the zipper algorithm[111, 108, 109, 110].

3.5.1 Zipper Algorithm

Let us take a driving function ζ_t for $t \in [0, t_n) : 0 = t_0 < t_1 < t_2 < ... < t_n$. The conformal map g_t is solution of the Loewner's equation for ζ_t, mapping $\mathbb{H} \setminus \gamma_{t_k}$ onto $\mathbb{H}$. We can convenient define a function G_k which maps $\mathbb{H} \setminus \gamma_{t_k - 1}$ onto $\mathbb{H} \setminus \gamma_{t_k}$,

$$G_k = g_{t_k} \circ g_{t_{k-1}}^{-1} \qquad , \tag{3.9}$$

and, therefore, the solution of Loewner's equation can be written as

$$g_{t_k} = G_k \circ G_{k-1} \circ G_{k-2} \circ ... \circ G_2 \circ G_1 \qquad . \tag{3.10}$$

The function G_k is not a solution of Loewner's equation because the trace generated, after the map, does not start at the origin, as we illustrate in the Fig. 3.3 (In Fig. 3.3 the function g_{t_1} and g_{t_2} are G_1 and G_2, respectively). To fix that, it is defined a new function,

$$g_k = G_k(z + \zeta_{t_{k-1}}) - \zeta_{t_{k-1}} \qquad , \tag{3.11}$$

which has a shift by $\zeta_{t_{k-1}}$ to relocate the trace to the origin. Then, just to be more precise, g_k is obtained by solving the Loewner equation with shifted driving function $\bar{\zeta}_{\Delta t_k} = \delta_k = \zeta_k - \zeta_{k-1}$ where $\Delta t_k = t_k - t_{k-1}$. So, this conformal map takes $\mathbb{H}$ minus a cut starting at the origin onto $\mathbb{H}$. So, if one is interested in extracting the trace, it is necessary to take the inverse of g_k

$$g_k^{-1}(z) = G_k^{-1}(z + \zeta_{t_{K-1}}) - \zeta_{t_{k-1}} \tag{3.12}$$

which takes $\mathbb{H}$ and introduces a cut which begins at the origin. The $k - th$ point of the curve is found by

$$\gamma_{t_k} = g_1^{-1}(...g_{k-1}^{-1}(g_k^{-1}(\delta_k) + \delta_{k-1})... + \delta_1) \tag{3.13}$$

Finally, we can extract the trace,

$$\gamma_k = h_1 \circ h_2 \circ ... \circ h_k(0) \tag{3.14}$$

where $h_k = g_k^{-1}(z + \delta_k)$.

We approximate the driving function on the interval $[t_{k-1}, t_k]$ by a function for which the Loewner equation may be explicitly solved. So, the maps G_k and g_k can be found explicitly and then, by the iteratively equation 3.10 we can approximate g_k to g_t. The form of h_k, however, is dependent on the interpolation drive δ_k that can be any analytical solution. However, we will consider the explicit solution refereed 'vertical slits'[108, 109, 110]. Vertical slit corresponds to a simple solution of the Loewner equation. Since the driving function does not start at 0, the curve will not start at the origin. The curve is just a vertical slit from δ_k to $\delta_k + i2\sqrt{\Delta t}$. Using vertical slits means that we approximate the driving function by a discontinuous piecewise constant function, and for the limit $\Delta t \to 0$, the generated trace converge to an SLE trace. Then, h_k has the form [109, 110]

$$h_k(z) = \delta + i\sqrt{4\Delta t - z^2} \qquad . \tag{3.15}$$

As previously mentioned, we are interested to verify if SLE candidates are in fact SLE_k curves. For that, we need to use the inverse of the Eq.3.14

$$0 = h_k^{-1} \circ h_{k-1}^{-1} \circ ... \circ h_1^{-1}(\gamma_k) \qquad . \tag{3.16}$$

Then, the conformal map $h_k^{-1} \circ h_{k-1}^{-1} \circ ... \circ h_1^{-1}$ sends $\mathbb{H} \setminus \gamma_k$ onto $\mathbb{H}$. As the vertical slit maps the origin to $\delta_k + i2\sqrt{\Delta t}$, that is,

$$h_k(0) = \delta_k + i2\sqrt{\delta t} \qquad , \tag{3.17}$$

so, by Eq. 3.16 and Eq. 3.17, we can write,

$$\omega_k = \delta_k + i2\sqrt{\delta t} = h_k^{-1} \circ h_{k-1}^{-1} \circ ... \circ h_1^{-1}(\gamma_k) \quad , \tag{3.18}$$

where ω_k means the map of such piece of the trace γ_k onto the border of $\mathbb{H}$. Then t_k and ζ_{t_k} are easily determined

$$t_k = \frac{1}{4}\sum_{i=1}^{k} Im\{\omega_i\}^2, \qquad \zeta_{t_k} = \sum_{i=1}^{k} Re\{\omega_i\} \quad , \tag{3.19}$$

with

$$\omega_k = h_{k-1}^{-1} \circ h_{k-2}^{-1} \circ ... \circ h_1^{-1}(\gamma_k) \quad , \tag{3.20}$$

and, taking the inverse of the Eq.3.15,

$$h_k^{-1}(z) = i\sqrt{-Im\{\omega_i\}^2 - (z - Re\{\omega_i\})^2} \quad . \tag{3.21}$$

Surprisingly, the effective algorithm is quite easy to implement. In summary, the analyzes of the SLE candidates curves, we will perform in the next section, from a such candidate γ in a upper half plane consist to calculate ω_k iteratively (Eq. 3.18). Finally, from the real term of ω_k, the next step is to calculate the driving function ζ_{t_k} and, from its imaginary term, calculate the SLE time t_k.

Given that, even for curves with equal length and step sizes, the discretized times t_k are not equally distributed, we linearly interpolate the measured driving function at equally spaced time intervals.

3.6 Results

Our main goal is to study the properties and symmetries of the complete perimeter of the percolation cluster extracted from correlated landscapes with H in the interval $[-1, 0]$. In Fig. 3.6 we show examples of complete perimeters and their respective driving functions. So far,

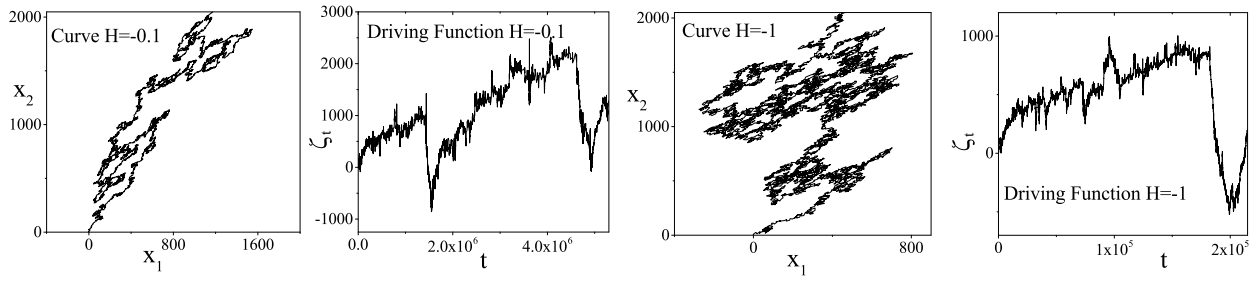

Figure 3.6: Examples of full perimeters of percolating cluster for $H = -0.1$ and $H = -1$ and their respective driving function, calculated by the zipper algorithm. The jumps of the driving function reproduce the sinuosity of its respective curve.

analytical results for the critical exponents have been obtained only in the cases where $H = -1$ (uncorrelated surface) and $H = 0$. Schrenk *et al.* [47] conjectured the following functional form for the H-dependence of the complete perimeter fractal dimension:

$$d_f = \frac{3}{2} - \frac{H}{3}, \quad H \in [-3/4, 0] \quad , \tag{3.22}$$

and was accurately reproduced by us, based on different distributions of $u(\mathbf{q})$. In Fig. 3.7 we present our numerical results for the H-dependece of the complete perimeter for $u(\mathbf{q})$ Gaussian distributed (as shown also in Fig. 2.4). As a result of section 2, the H-dependence was shown to be independent of the shape of the distribution of the two-dimensional random numbers, $u(\mathbf{q})$, used to generate the correlated landscapes [12].

In the case where the random curve is SLE in the scaling limit, the resulting driving function is a Brownian motion with mean square displacement that scales with time as

$$\left\langle \zeta_t^2 \right\rangle \sim \kappa t. \tag{3.23}$$

We therefore investigate this dependence for critical site percolation interfaces of random landscapes with H values in the interval $[-1, 0]$. As shown in Fig. 3.8, we have obtained a good linear dependence of the variance on time. The different slopes (κ values) are due to the different Hurst exponents of the random surfaces from where the curves were extracted. The mean square displacement error $\Delta \left\langle \zeta_t^2 \right\rangle$ was defined as the fourth momentum of the driving function,

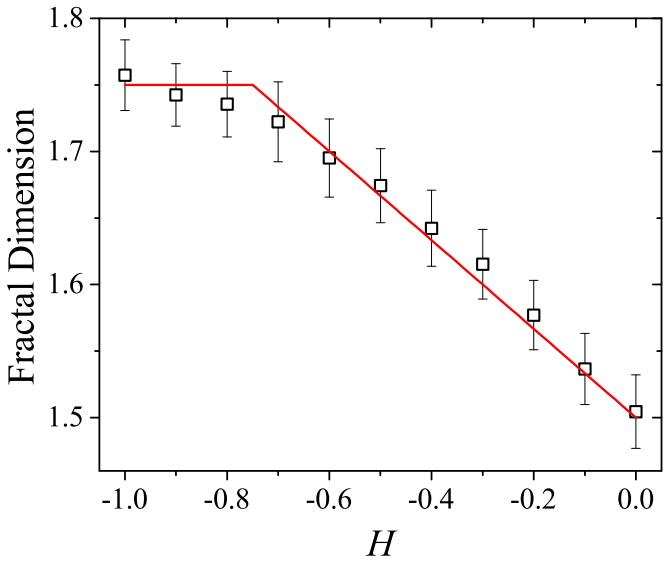

Figure 3.7: Fractal dimension of the full perimeter as a function of H, calculated via yardstick method[12]. The red line represent a conjecture proposed by Schrenk *et al.*[47]. All values are averages over 10^4 samples and the error bars are defined by the variance of the distribution of the fractal dimension values.

computed as follows:

$$\Delta\left\langle\zeta_t^2\right\rangle = \sqrt{\frac{1}{N}\left[\left\langle\zeta_t^4\right\rangle - \left\langle\zeta_t^2\right\rangle^2\right]}, \qquad \left\langle\zeta_t^4\right\rangle = \frac{1}{N}\sum_{k=1}^{N}\zeta_t^4, \tag{3.24}$$

where N is the total number of samples of driving functions.

In order to determine the value of κ we first made a second order polynomial fit of the data for the time evolution of $\langle\zeta_t^2\rangle$ (Fig. 3.9). We then took the derivative of $\langle\zeta_t^2\rangle$ at each time step, as shown in the inset of Fig. 3.9. Using κ_{max} and κ_{min} to denote respectively the maximum and minimum values of κ, we estimated κ and its corresponding error with the following expression:

$$\kappa = \left(\frac{\kappa_{max} + \kappa_{min}}{2}\right) \pm \left(\frac{\kappa_{max} - \kappa_{min}}{2}\right). \tag{3.25}$$

Following Equation 3.25, we calculated κ for a family of curves associated with different values of H. The results are shown in figure 3.10. Combining the conjecture in equation 3.22 and

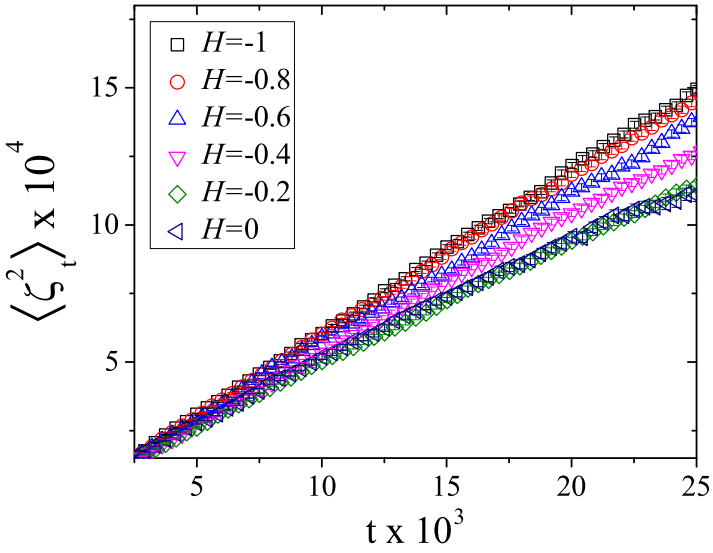

Figure 3.8: The linear time dependence of the mean square displacement of the driving function for different values of Hurst exponent. Without loss of information, in this plot we did not show all the data points used for the full calculation of the κ. All values are average over 10^4 samples and the error bars (inside the symbols) are defined by the variance of the mean square displacement distribution of the driving function.

equation 3.7, one may write the functional dependence of κ on H as follows:

$$\kappa = 8\left(\frac{1}{2} - \frac{H}{3}\right). \tag{3.26}$$

As shown in the figure 3.10 the conjecture in equation 3.26, represented by the red curve, is in good agreement with the values of κ estimated by the zipper algorithm.

In order to confirm that a random curve is SLE it is not sufficient that the evolution of the means square displacement of the corresponding driving function is linear in time as shown in figure 3.9. It is also necessary that the driving function is uncorrelated in time. We therefore tested for the Markov property of the driving function by computing its time correlation function $c(t,\tau)$, defined by:

$$c(t,\tau) = \frac{\langle \zeta_{t+\tau}\zeta_t\rangle - \langle \zeta_{t+\tau}\rangle \langle \zeta_t\rangle}{\sqrt{\left(\langle \zeta_{t+\tau}^2\rangle - \langle \zeta_{t+\tau}\rangle^2\right)\left(\langle \zeta_t^2\rangle - \langle \zeta_t\rangle^2\right)}}. \tag{3.27}$$

As shown in Fig. 3.11 the correlation $c(t,\tau)$ goes to zero after a few times steps, as expected for Brownian motion. The short time correlation is associated to the discretization of the curve, i.e. due to the finite grid size. For completeness in the investigation of Markov property we also calculated the distribution of the driving function for a specific time (t^*), which is shown

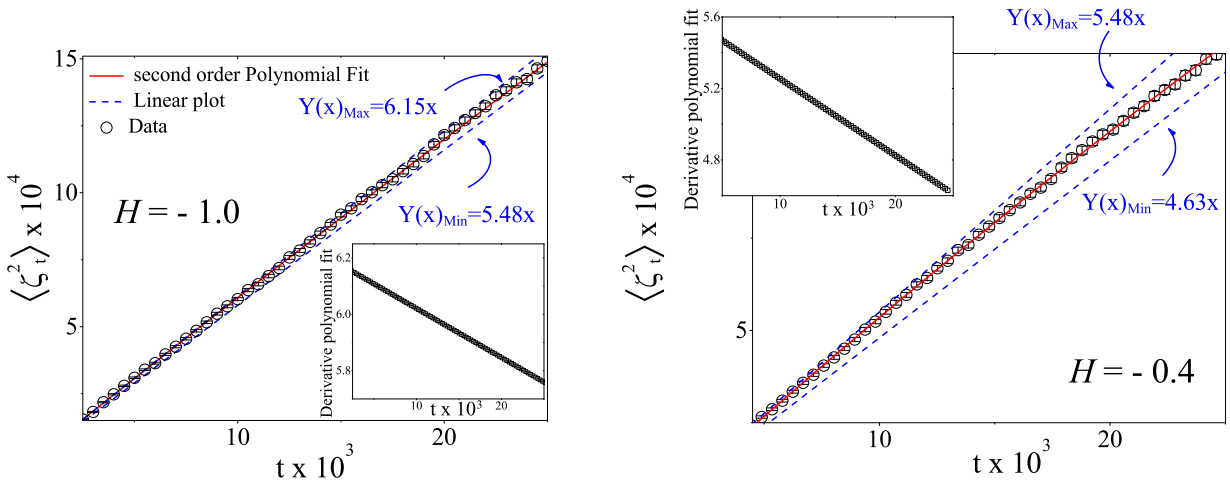

Figure 3.9: The linear time dependence of the mean square displacement of the driving function for different Hurst exponents. The red line corresponds to the second order polynomial fit ($y = b_1x^2 + b_2x + c$, where $b_1 \in [10^{-6}, 10^{-5}]$, b_2, c are real numbers). The dashed blue lines represented by $Y_{Max}(x)$ and $Y_{Min}(x)$ are lines with the maximum and minimum slope (κ) calculated by taking the derivative of the mean square displacement (see inset).

to follow a Gaussian distribution (see inset of Fig. 3.11).

Conclusion

Given that many systems can be viewed as long-range correlated landscapes, properties of the iso-height lines extracted from them become relevant. Our results suggest that the complete perimeter of the percolating cluster of long-range correlated landscapes ($-1 \leq H \leq 0$) are statistically equivalent to SLE curves. We found consistent agreements between the diffusion constant κ calculated by the zipper algorithm and the κ calculated via the fractal dimension of the SLE curves[106]. In addition, we also showed that in the scaling limit the curves are Markovian in nature, in the sense that their driving functions are uncorrelated in time and Gaussian distributed at specific points in time. Having established that the curves under study are indeed SLE allows us to extend the established results from SLE to iso-height lines and to generate an ensemble of such curves just solving a stochastic differential equation, without the need to generate the entire landscape.

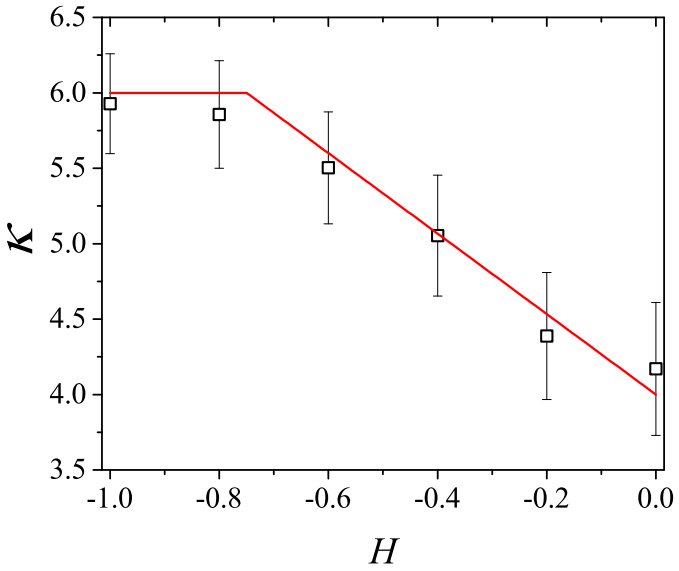

Figure 3.10: Dependence of diffusion coefficient (κ), estimated by equation 3.25, on Hurst exponent (H). The red line is the conjecture described by equation 3.26. The H-dependence of κ shows agreement, into the error bars, with κ related to the full perimeter of the percolating cluster.

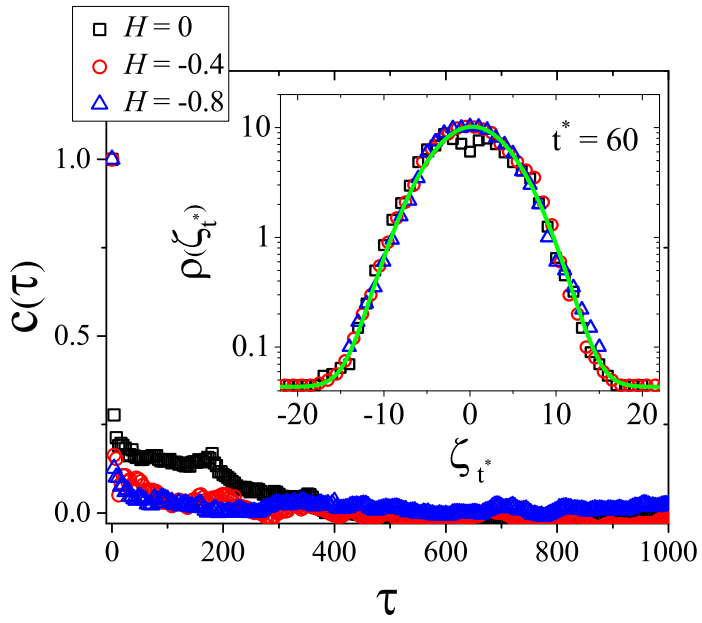

Figure 3.11: Correlation time of the driving function for three different values of Hurst, $H = -0.8, -0.4, 0$.The inset shows the probability density distribution $\rho(\zeta)$ for a specific Loewner time $t^* = 60$ for the same Hurst values described above. The solid green line is guide to the eye $\rho(\zeta) = \frac{1}{\sqrt{2\pi\kappa t^*}} \exp\left(\frac{-\zeta_{t^*}^2}{2\kappa t^*}\right)$.

Chapter 4

Fowler-Nordheim Theory

The main purpose of field electron emission theory is to find out the current-field characteristic of field emission. The Fowler-Nordheim (FN) theory is an elementary field electron emission theory. Fowler and Nordheim gave an analytic formula on the emission current density, based on a simplified field electron emission model and a series of assumptions. Actually, by using the series of assumptions in an elementary field emission model, one can, analytically or approximately, solve the field emission problem deriving then the dependence of the emission current density on electric field, $J - F$. The basic concepts and methods of the FN theory enable us to understand the basic behavior of field emission. Therefore, they are just a starting point of the field emission theory for more complicated field emission systems, such as semiconductors, surface, impurity effects, and nanowires.

There is no connection between the symbols used in the next sections with those defined in the previous Chapters.

4.1 General Physical Assumptions

The general assumptions of the FN physical model are as follows [112]:

- the emitter has a smooth surface from the microscopic point of view (this approxima-

tion enables us to catch the bulk properties in field emission even though the effects of impurities, defects and geometric shape of emitter could play some role in the field emission);

- there exist a uniform electric field F external to the emitting surface;
- the work function ϕ is independent of the external electric field because the electric field cannot penetrate into the metal. However, for semiconductors and nanomaterials, such as CNTs, electric field could penetrate into them;
- the potential energy in which an electron moves is given by a Sommerfeld-type model, modified by the external electric field (Sommerfeld-type models are 'free-electron' models that assume no interaction between electrons, or between electrons and individual ion cores);
- electrons emission is in an equilibrium state obeying Fermi-Dirac statistics;
- almost all emitted electrons are able to tunnel through the potential barrier.

There exist different methods to derive the same field emission equation. As examples are Fowler-Nordheim's method, Morphy-Good's method, Young-Gadzuk's method, Haug's method and Forbes's method[112]. Even though they use different ways to integrate in the energy range, all of these methods will give the same field emission equation. However, when one generates these methods to more complicated field emission models, one should choose the method carefully and mind about the different approximations.

4.2 Local Current Density Type Equation

In this section we will derive the electron emission current density for a metal following the assumptions previously pointed out.

4.2.1 Energy-space Diagrams

How to analytically derive the emission current density for a general potential barrier is still a challenging problem. However, it can be solved by a combination of Schrödinger and Poisson equations from the first-principles point of view. In principle, the vacuum potential barrier should be three-dimensional and present couplings between dimensions, x-direction coupled with $y-z$ directions. Also, the vacuum potential barrier depends on the applied electric field, the shape of emitter (because the geometry of surface of metal can modify the local electric field distribution of emitter), the work function and the energy band structure of emitter (because the matching between emitter and vacuum induces the coupling of the energy band of the emitter and vacuum potential barrier). However, most of field emission devices can be approximately regarded as the decoupling between different directions, by following the previous assumptions.

The main issue is then to find out the relationship between the emission current and external field and the energy distribution of the electrons. For this, cold field electron emission (CFE) theory involves calculation of the escape probability[1] D for an electron approaching the emitter surface in a given internal electronic state, and then perform summation over all occupied states to give the emission current density J. Hence, the potential coupling between different directions can be ignored and, therefore, the problem of transmission coefficient can be reduced to the one-dimensional Schrödinger equation.

Lets consider E as the total energy, relative by to some arbitrary zero, and K the kinetic energy. Therefore, the total energy value at the conduction band is E_c and at the top of the potential energy step is E_0. The local well depth is denoted by $\chi_c = E_0 - E_c$ and the work function $\phi = E_0 - E_F$, where the total energy of the topmost filled state relative to E_c at $0K$ is the Fermi energy E_F, as illustrated by fig. 4.1. The energy relative to the conduction band base, for a free-electron model, is the kinetic energy in nature as $K = E - E_c$. Thereby the total electron energy relative to the Fermi level, $\varepsilon = E - E_F$, and the Fermi kinetic energy is $K_F = E_F - E_C$. After all these definitions, it is clear that such kinetic electron energy K and

[1] Also called transmission probability or tunneling probability.

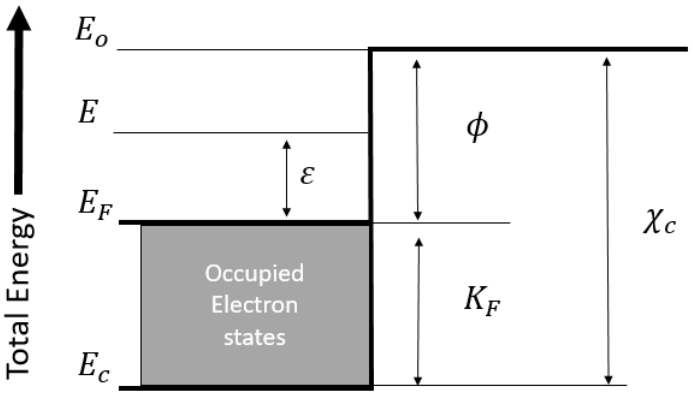

Figure 4.1: Electron energy diagram in the context of Sommerfeld model.

ε are related by

$$K = E - E_c = (E - E_F) + (E_F - E_c) = \varepsilon + K_F \tag{4.1}$$

and E and ε are related by

$$E = E_0 + (E_F - E_0) + (E - E_F) = E_0 - \phi + \varepsilon \quad . \tag{4.2}$$

In the Sommerfeld model, the total energy summation is particularly straightforward, with the parallel p and normal n component equation to the emitter surface. Any of these components can be used to describe the electrons energy in a CFE approach. As we will show below we will mainly work with the parallel-energy component[2]. In a free-electron model, the component of electron momentum parallel to the emitter surface may be conserved because its solutions are applicable inside the emitter, in the barrier region and in the vacuum. For motion normal to the surface we associate E_n given by $E_n = E - K_p$, where E_n is the normal energy, K_p and E_n are the eigenenergies for the parallel and normal motion, respectively. So, from Eq. 4.2,

$$E_n = E_0 - \phi + \varepsilon - K_p \equiv E_0 - V_h \tag{4.3}$$

where V_h is called the unreduced barrier height (barrier height when there is no external electric

[2]When we say parallel-energy or normal-energy component, we refer to the energy associated to the component of electron momentum to the emitter surface.

field applied) as,

$$V_h \equiv \phi - \varepsilon + K_p \quad . \tag{4.4}$$

with,

$$\left(\frac{\partial V_h}{\partial \varepsilon}\right)_{K_p} = -1 \quad , \quad \left(\frac{\partial V_h}{\partial K_p}\right)_{\varepsilon} = 1 \quad . \tag{4.5}$$

Based on the 'T-type' energy-space diagram for a free-electron metal conduction band, as shown in figure 4.2, and with suitable approximations we will can the electron current density equation.

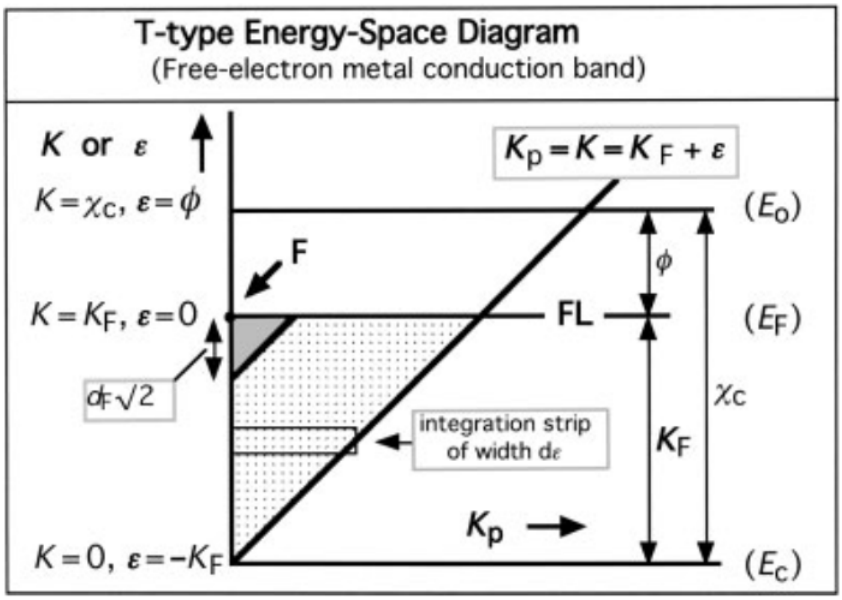

Figure 4.2: 'T-type' energy-space diagram for a free-electron metal conduction band. The vertical axis is the total energy ε and the horizontal axis is the component K_p of the kinetic energy parallel to emitter surface. This scheme is from Forbes's reference [114]. The heave shaded region, a triangle of side-length $d_f\sqrt{2}$ where d_f defines the decay width, is where the tunneling electrons drawn from. This because one rough requirement for Eq. 4.30 (see below) to be valid is that $K_F > d_F\sqrt{2}$.

The horizontal axis represents the parallel component K_p of the electron kinetic energy while the vertical axis represents the total electron energy. The label F represents a state on the emitter surface with total energy $E = E_F$ (i.e. $K = K_F$ or $\varepsilon = 0$). On the diagrams, one can draw a region ($K > 0$ and $K_p \leq K$) where solutions of the Schrödinger equation can be found: each element in this region (dotted area) represents a class of equivalent solutions that (for a free-electron model) have identical properties with respect to the electron emission.

Let us denote Z as the electron current density crossing a surface in space inside the free electron metal. So, as shown in the diagram (figure 4.2), the contribution d^2Z to Z that comes from the energy-space element $dK_p dK_n$ is [113, 114]

$$d^2Z = z_s f dK_p dK_n = z_s f dK_p d\varepsilon \tag{4.6}$$

where f is the occupation probability for the states in question and z_S is a universal constant inherent in Sommerfelds work [115], given by

$$z_s = 4\pi em/h_p^3 \approx 1.618311 \times 10611 Am^{-2}eV^{-2} \tag{4.7}$$

The contribution d^2J to the emitted electron current density (ECD) J is

$$d^2J = Dd^2Z \tag{4.8}$$

where D is the electron escape probability. It follows that J is given integrating over the total energy distribution as,

$$J = z_s \int\int f D dK_p dK_n \tag{4.9}$$

and,

$$J = z_s \int\int f D dK_p d\varepsilon \qquad . \tag{4.10}$$

In both cases, the double integral is taken over the domain of energy space where occupied electron states exist. As we are considering the thermodynamic equilibrium conditions, f is the Fermi-Dirac occupation f_{FD} and depends only of ε. So, the integral 4.10 reduces to

$$j(\varepsilon) = z_s f_{FD} \int D dK_p \tag{4.11}$$

$$J = \int j d\varepsilon \tag{4.12}$$

where $j(\varepsilon)$ is the total energy distribution of the emitted electrons. Now it is necessary to approximate D as a suitable function of ε and K_p, as we will show below.

4.2.2 Gamow Exponent - Approximation of the Escape Probability

The Schrödinger equation in the x direction (perpendicular direction to the emitter) is,

$$-\frac{\hbar^2}{2m_e}\frac{d^2\psi_{inc}}{dx^2} = E_x\psi_{inc} \qquad for \quad x \leq 0 \tag{4.13}$$

$$-\frac{\hbar^2}{2m_e}\frac{d^2\psi_{tra}}{dx^2} + V_b\psi_{tra} = E_x\psi_{tra} \qquad for \quad x > 0 \tag{4.14}$$

where ψ_{inc} and ψ_{tra} stand for the incident and transmitted wave function, respectively, V_b is the potential energy for the emitted electrons, m_e is the electron mass and $\hbar = h/2\pi$ where h is the Planck constant. Here, $x = 0$ represents the edge of the Sommerfeld well. If V_b is assumed to be the triangular barrier, $V_b = V_h - eFx$, one can solve Schrödinger's equation exactly [112].

However, for similar barrier shapes, extensive mathematical research from the early 1800s onward still did not find out a simple exact solutions for such Schrödinger equation. Thus, approximate solutions have been sought and a large mathematical work exists on Jeffries-Wentzel-Kramers-Brillouin (JWKB)-type solutions [112].

The JWKB method is a mathematical method for finding approximate solutions of linear differential equations with spatially varying coefficients in mathematics physics. It is often used for a semiclassical calculation in quantum mechanics in which the wave function is written as an ansatz of an exponential function, and semiclassically expanded. Either the amplitude or the phase is taken to be slowly changing. For most electrons, emitted in a CFE regime, the tunneling barrier is sharp and strong. This means that the most appropriate correct JWKB-type formula for the escape probability is the Landau and Lifschitz formula defined as [116, 117, 118],

$$D = P\exp\left[-G(V_b^{'})\right] \tag{4.15}$$

where P is a 'tunneling pre-factor' and $G(V_b^{'})$ is the so-called JWKB exponent or even Gamow exponent,

$$G(V_b^{'}) = g_e\int\sqrt{V_b^{'}}dx \qquad , \tag{4.16}$$

integrated between the classic turning points (see fig. 4.3). The JWKB constant for an electron is $g_e \equiv (8m)^{1/2}/\hbar \cong 10.24634\ eV^{1/2}\ nm^{-1}$[114] is a constant for electron tunneling. The pre-factor P is presumed varying slowly with the barrier height V_h in comparison with $exp\left[-G(V_b^{'})\right]$ and also it may differ only a little from unity [114, 112]. In practice sets $P = 1$ so,

$$D \approx \exp\left[-G(V_b^{'})\right]. \tag{4.17}$$

As soon as E_n is at the the Fermi level E_F, consequently $V_h = \phi$ and $G(V_b^{'})$ can be Taylor-expanded as,

$$G(V_b^{'}) = G(\phi + \delta V_h) = G(\phi) + \frac{\delta V_h}{d_F} + ... \qquad , \tag{4.18}$$

where d is a parameter with dimensions of energy called the decay width [119],

$$d_F^{-1} = \left(\frac{\partial G}{\partial V_h}\right)_F \qquad . \tag{4.19}$$

Due to the considered assumptions, the standard CFE theory uses only the linear term [114, 112] so the Eq. 4.18 can be written,

$$G \approx G_F + \frac{\delta V_h}{d_F} \tag{4.20}$$

where $G_F = G(V_h = \phi) = G(\varepsilon = E_p)$ and the escape probability takes the form,

$$D(V_b) \approx exp\left(-G_F - \frac{\delta V_h}{d_F}\right) \approx D_F \exp\left(-\frac{\delta V_h}{d_F}\right) \qquad , \tag{4.21}$$

where $D_F = exp(-G_F)$. By the Eq. 4.4 and Eq. 4.5 we can express δV_h in terms of ε and K_p, such that,

$$\delta V_h = \left(\frac{\partial V_h}{\partial \varepsilon}\right)_{K_p} \delta\varepsilon + \left(\frac{\partial V_h}{\partial K_p}\right)_{\varepsilon} \delta K_p = -\delta\varepsilon + \delta K_p \qquad . \tag{4.22}$$

So, when we expand D relative to the F state we can write,

$$\delta V_h = -\varepsilon + K_p \tag{4.23}$$

and therefore

$$D \approx D_F \exp\left(\frac{\varepsilon}{d_F}\right) \exp\left(\frac{-K_p}{d_F}\right) \quad . \tag{4.24}$$

It is valid to emphasize that this result has been proved only for a free-electron model and usually will not be exactly valid for more-advanced models.

4.2.3 Emission Current Density Equation

Finally, once D was expressed in terms of ε and K_p, we used the approximation 4.24 into Eq. 4.11 such that,

$$j(\varepsilon) \approx z_s f_{FD} D_F exp\left(\frac{\varepsilon}{d_F}\right) \int_0^{K_F+\varepsilon} \exp\left(-\frac{K_p}{d_F}\right) dK_p \tag{4.25}$$

which is an integral in energy space over the horizontal axis in fig.4.2 from $K_p = 0$ to $K_p = K = K_F + \varepsilon$. From this simple integrations one gets

$$j(\varepsilon) \approx z_s f_{FD} D_F d_F \left[\exp\left(\frac{\varepsilon}{d_F}\right) - \exp\left(-\frac{K_F}{d_F}\right)\right] \quad . \tag{4.26}$$

For a metal the conduction band said as 'deep', that means K_F is significantly greater than d_F, such that we may neglect the exponential term $exp\left(-\frac{K_F}{d_F}\right)$ in Eq. 4.26, what leads to the form,

$$j(\varepsilon) \approx z_s f_{FD} D_F d_F exp\left(\frac{\varepsilon}{d_F}\right) \quad . \tag{4.27}$$

So, the emission current density J is obtained by integrating Eq. 4.12. This integration is over up the vertical axis of the diagram shown in fig. 4.2. At 0 temperature, $f_{FD} = 1$ for $\varepsilon = 0$ and $f_{FD} = 0$ for $\varepsilon > 0$, so the states contributing, in principle, to the zero-temperature emission current density are those in the large shaded triangular domain in the fig. 4.2. Thus,

$$J \approx z_s d_F D_F \times \int_{-K_F}^{0} exp\left(\frac{\varepsilon}{d_F}\right) d\varepsilon \tag{4.28}$$

$$\approx z_s d_F^2 D_F \left[1 - exp\left(\frac{K_F}{d_F}\right)\right] \quad , \tag{4.29}$$

and as K_F is significantly greater than d_F (the same approximation as in Eq. 4.26), we finally obtain

$$J \approx z_s d_F^2 D_F \quad . \tag{4.30}$$

Results for specific barrier shapes are obtained by deriving values for the corresponding Gamow exponents. The elementary triangular barrier has a special status because there is a simple analytical result to which formulae for other quasi-triangular barriers can be related by correction factors.

For a typical elementary triangular barrier, the vacuum potential barrier, $V_b = V_h - eFx = \phi - \varepsilon + E_p$, by using the JWKB method and notice that $G_F = G(\varepsilon = E_p)$ (i.e., height for zero applied field F), the Gamow exponent is given by (Eq. 4.16),

$$G^{el} = \frac{b\phi^{3/2}}{F} \tag{4.31}$$

where b is the second Fowler-Nordheim constant, $b \equiv (2/3e)g_e = (4/3)(2m)^{1/2}/e\hbar_p \cong 6.830890$ $\mathrm{eV}^{-3/2}\ V\ nm^{-1}$ [114].

It follows, from Eq. 4.17, 4.19 and 4.31, that

$$D_F^{el} = exp\left(-b\phi^{3/2}/F\right) \tag{4.32}$$

$$d_F^{el} = (2/3)b^{-1}\phi^{-1/2}F \quad . \tag{4.33}$$

where the label '*el*' is related to the triangular elementar barrier. Using the definition of z_s (Eq. 4.7) and substituting the second FN constant b into Eq. 4.33, one is able to find the remaining part of the emission current density J (Eq. 4.30)

$$z_s(d_F^{el})^2 = a\phi^{-1}F^2 \tag{4.34}$$

where a is the 'first Fowler-Nordheim constant'[114],

$$a \equiv e^3/8\pi h_p \cong 1.541433 \times 10^{-6} AeVV^{-2} \quad . \tag{4.35}$$

Then, the emission current density for an elementary barrier, at 0 temperature, is

$$J^{el} = a\phi^{-1}F^2 exp\left(-b\phi^{3/2}/F\right) \quad . \tag{4.36}$$

However, since the electron emission arises at the tip of the emitter, we consider an electron inside the metal seeing a constant (zero) potential, which induces effectively the image potential near the metal surface from classical electrodynamics. Such barrier, which considers this correlation-and-exchange effects, is known as Schottky-Nordheim (SN) barrier, assuming its standard form as,

$$V_b = \phi - eFx - \frac{e^2}{16\pi\epsilon_0 x} \tag{4.37}$$

where, eFx is the electrostatic term and the term $e^2/16\pi\epsilon_0 x$ models the correlations-and-exchange effects by a classical image potential energy, as figure 4.3 shows. Due to the new term in the SN barrier, two special elliptic correction functions, ν_{SN} and τ_{SN}, arise when the simple-JWKB method is applied to solve the Schrödinger equation approximately [119], such that,

$$G^{SN} = \nu_{SN} G^{el} = \nu_{SN} b\phi^{3/2}/F \tag{4.38}$$

and, consequently, the escape probability is written as,

$$D_F^{SN} = \exp\left(-\nu_{SN} b\phi^{3/2}/F\right) \tag{4.39}$$

and

$$d_F^{SN} = \tau_F^{SN} d_F^{el} \tag{4.40}$$

where

$$\tau_F^{SN} \equiv \nu_{SN} + \frac{2}{3}\phi\left(\frac{\partial \nu_{SN}}{\partial \phi}\right) \quad . \tag{4.41}$$

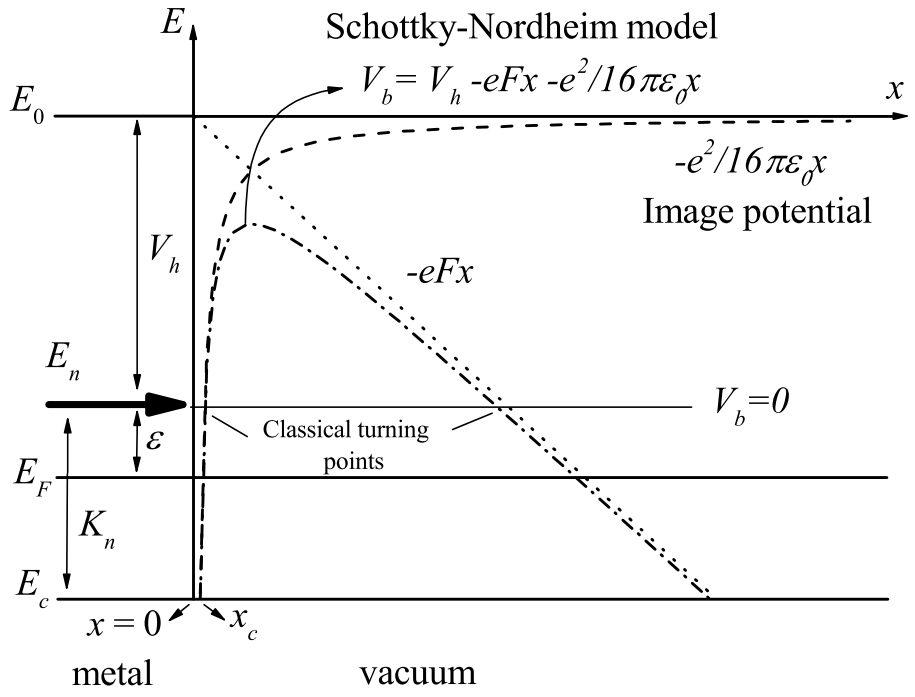

Figure 4.3: Potential energy experienced by an electron tunneling, the Schottky-Nordheim tunneling barrier. when a model potential energy goes strongly negative as x tends to zero, and dips below the conduction-band base for $x < x_c$, and therefore for such interval $V_B = V_h - \chi_c$.

Then, the resulting form of the Fowler-Nordheim equation is written as,

$$J = a\phi^{-1}F^2\tau_F^{-2}exp\left(-\nu_{SN}b\phi^{3/2}/F\right) \tag{4.42}$$

In the next sections we will discuss the importance of the functions ν_{SN} and τ_{SN}.

4.2.4 Approximations for the Special Elliptic correction functions

In this section we are going to report a good approximation for the correction functions that appear in the Eq. 4.42, due to the consideration of the Schottky-Nordheim (SN) barrier. As describe in the previous section, Fowler and Nordheim published their seminal paper on CFE theory but they knew that the triangular tunneling barrier was physically unrealistic. The SN barrier describes better the tunneling phenomenon, but for this barrier the Schrödinger equation has no exact analytical solutions. From JWKB-approximation method the functions ν_{SN} and τ_{SN} have been derived which are purely mathematical definitions that depend only on

a single variable y, such that

$$\nu_{SN}(y) = (1+y)^{(1/2)}[E(m) - yK(m)] \tag{4.43}$$

where $m = \frac{1-y^{1/2}}{1+y^{1/2}}$ and $y = \left(\frac{1-m}{1+m}\right)^2 = \left(\frac{e^3}{4\pi\varepsilon_0}\frac{F}{V_h^2}\right)$. $E(m)$ and $K(m)$ are well-know complete elliptic integrals [112],

$$E(m) = \int_0^1 (1-z^2)^{(-1/2)}(1-mz^2)^{1/2}dz \tag{4.44}$$

$$K(m) = \int_0^1 (1-z^2)^{(-1/2)}(1-mz^2)^{-1/2}dz \quad . \tag{4.45}$$

An important contribution came by Forbes[120], showing that the correction factor obeys the differential equation,

$$y(1-y)\frac{d^2\nu_{SN}}{d\nu_{SN}^2} - \frac{3}{4}\nu_{SN} = 0 \tag{4.46}$$

by the series solution

$$\nu_{SN}(y) \approx 1 - y + \frac{1}{6}y\ln(y) \quad . \tag{4.47}$$

and

$$\tau_{SN}(y) \approx 1 - \frac{1}{9}y + \frac{1}{18}y\ln(y) \quad . \tag{4.48}$$

In CFE theory y has been the Nordheim parameter y, such as

$$y \equiv \frac{\Delta_s}{V_h} \quad . \tag{4.49}$$

$\Delta_s = cF^{1/2}$ was shown by Schottky [121] as being amount in energy by which the top of the image-potential- reduced barrier has been lowered from V_h for a field F (see the fig. 4.4). Therefore we may write,

$$y = \frac{cF^{1/2}}{V_h} \quad . \tag{4.50}$$

Forbes and Deane [116, 122, 119, 123] have discussed this point in details and showed that, from mathematical and physical reasons a good approximation for $y^2 \equiv f$, $\nu_{SN} \equiv \nu_{SN}(y^2) \equiv \nu_{SN}(f)$

$$\nu_{SN}(f) \approx 1 - f + \frac{1}{6}f\ln(f) \quad . \tag{4.51}$$

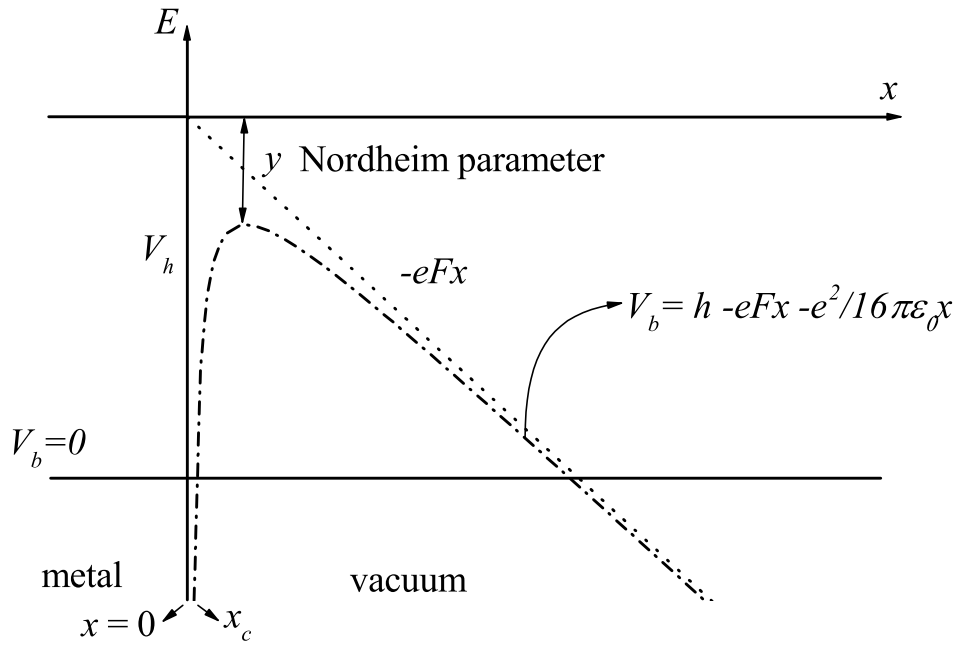

Figure 4.4: Illustration of the SN barrier.

The parameter f was introduced by Forbes [120], named 'scaled barrier field", which is the ratio of the electric field that defines a tunnelling barrier to the critical field needed to reduce barrier height to zero, written as,

$$f = \frac{F}{F_R} = \frac{c^2 F}{V_h^2} \tag{4.52}$$

where $F_R = V_h^2/c^2$ is the field needed to reduce a barrier height from V_h to zero. When V_h is the local work function ϕ, then F_R becomes F_ϕ^{SN}, at which the SN barrier for a forward-moving Fermi-level electron vanishes.

The approximation 4.51 outperforms all earlier approximations of equivalent complexity [124] and gave, for the first time, a simple and reliable algebraic approximation for ν in the standard FN-type equation. Also, Forbes [120] has defined an important physical quantity, f, which have introduced physical meaning into the mathematical assumptions to determine the form of ν_{SN}.

We have been considering only ν_{SN} because τ_{SN} will be grouped together with another correction factor into the pre-exponential corrector factor, λ, defined below.

4.3 Large Area Field Emitters

For the n-th individual emitter of a large-area field emitter (LAFE), it is possible to associate a local characteristic macroscopic field enhancement factor (FEF), γ_n, that represents how the characteristic field F_n at its apex, if electrostatic interaction effects (usually referred to as shielding)[19] are negligibly small, is related to the applied electrostatic field F_M, i.e.,

$$\gamma_n \equiv \frac{F_n}{F_M}. \tag{4.53}$$

Thus, γ_n may depend on the gap length between the emitter and counter-electrode. For CFE applications, the interest arises when the gap length is much greater than the maximum height of the most protruding emitter. In the case, γ_n depends only on the geometry of the system[1,16,17]. For large-area emitters formed by multiwall CNTs, Bonard et al.[6] showed that only the sites with the highest characteristic macroscopic FEFs contribute to the emitted current. This aspect allows one to define a characteristic macroscopic FEF for the LAFE, γ_c, when assuming that the characteristic point C is formally taken at the apex of the emitter with the highest local apex FEF. We adopt this definition in the present work. Such macroscopic FEF is an important parameter that should be extracted experimentally because high γ_c values may indicate low turn-on field electron emission in the low applied electrostatic field regime.

The macroscopic (or LAFE average) emission current density J_M and the related parameters are then defined via,

$$J_M = \alpha_n J_c = \alpha_f \lambda_c J_{kc} \tag{4.54}$$

where α_n is the notional area efficiency, i.e., the ratio A_n/A_M, where A_n is the notional area and A_M is the whole macroscopic area (or "footprint") of the LAFE. The quantity α_f is the formal area efficiency, which corresponds to the ratio A_f/A_M, where A_f is the formal area [125, 30, 126]. In addition, J_c and J_{kc} correspond to the characteristic and kernel characteristic local current densities, respectively. These quantities are related by $J_c = \lambda_c J_{kc}$, where λ_c is the characteristic pre-exponential correction factor and it is not known for the present CFE experiments [116, 126]. This pre-exponential correction factor likely depends on the detailed electronic structure

of the material, the temperature, and the integration over the electronic states [116]. The parameter A_n is an estimate of the geometrical area that significantly emits electrons; however, the parameter extracted from a properly analyzed experimental measurement via, for example, an ordinary FN plot of type $\ln(J_M/F_M^2)$ vs $1/F_M$ [28], is A_f, which is different from A_n when λ_c is different from unity [125]. The best estimate is that λ_c lies in the range of $0.005 < \lambda_c < 11$ [28]. For convenience, we set $\lambda_c = 1$ for all simulations. The called Kernel current density for the SN barrier was introduced by Forbes [126] as,

$$J_{kc} = a\phi^{-1}F_c^2 exp\left(-\nu_{SN} b\phi^{3/2}/F_c\right) \quad . \tag{4.55}$$

where F_c is the local characteristic field. Because that all theoretical uncertainties associated with prediction of J_c is accumulated into the parameter λ_c, J_k^{SN} can be calculated exactly. Then, the Eq. 4.54 written as

$$J_M = \alpha_F \lambda_c \phi^{-1} F_c^2 exp\left(-\nu_{SN} b\phi^{3/2}/F_c\right) \tag{4.56}$$

is considered an FN-type equation because is 'technically complete', once it contains formal correction factors that are defined in such a way that all physical effects relevant to the dependent variable in use are encompassed within the equation. Fields, current densities, corrections factors and related parameters vary with position on an emitter and LAFE surface. The so-called characteristic values related to some specific position that is considered characteristic of the emitter and/or of the LAFE. We notice that one must be attentive when the quantities are the characteristic value of a single emitter/site or a characteristic value of the LAFE. As used before to define the LAFE, each γ_n is the characteristic FEF for a single emitter/site and, among the all emitter/sites the one which is the maximum FEF of the LAFE is labeled by characteristic of the LAFE. Thus, the J_c showed in the Eq. 4.54 is the emission current density associated to highest FEF of the LAFE.

So, considering that $\gamma_c = F_C/F_M$, if one puts γ_c into Eq. 4.42,

$$J_M = a\phi^{-1}\gamma_c^2 F_M^2 \alpha_f \exp\left(-\nu_{SN} b\phi^{3/2}/\gamma_c F_M\right) \tag{4.57}$$

$$\ln(J_M/F_M^2) = \ln(C) - \frac{\nu_{SN} B}{F_M} \tag{4.58}$$

where $C = a\phi^{-1}\gamma_c^2\alpha_f$, but it may depends on the other correction factors and $B = b\phi^{3/2}/\gamma_c$. The slope S^{SN} of the FN plot 4.58 can be written as [126]

$$S^{SN} = \frac{\partial\left[\ln(J_M/F_M^2)\right]}{\partial\left[1/F_M\right]} = -\sigma_t B \tag{4.59}$$

where the slope correction factor σ_t depends on various individual contributing factors which for our considerations is given by

$$\sigma_t = -\frac{\partial\left[ln(C)\right]}{\partial[1/F_M]} - \left[\nu_{SN} B + \frac{1}{F_M}\frac{\partial\left[\nu_{SN}\right]}{\partial[1/F_M]} B + \frac{1}{F_M}\frac{\partial\left[B\right]}{\partial[1/F_M]}\nu_{SN}\right] \quad . \tag{4.60}$$

or, dividing for $1/\beta_F$,

$$\sigma_t = -\frac{\partial\left[\ln(C)\right]}{\partial[1/F_M]}\frac{1}{B} - \left[\nu_{SN} + \frac{1}{F_M}\frac{\partial\left[\nu_{SN}\right]}{\partial[1/F_M]} + \frac{1}{BF_M}\frac{\partial\left[B\right]}{\partial[1/F_M]}\nu_{SN}\right] \quad . \tag{4.61}$$

As a common use of FN plots is to estimate the characteristic FEF γ_c, by Eq. 4.59 it is obtained by

$$\gamma_c = -\frac{\sigma_t b\phi^{3/2}}{S^{fit}} \tag{4.62}$$

where S^{fit} is the slope estimated from the FN plot. To obtain a predicted value for σ_t, one consider $\ln(C)$ and B constant by $1/F_M$, and to assume that no series-resistance-related effects occur. Forbes *et al.* [127] call this the basic approximation, and show that equation Eq. 4.61 then reduces to

$$\sigma_t = \nu_{SN} - F_c\frac{\partial\nu_{SN}}{\partial F_c} \tag{4.63}$$

As we have assumed that tunnelling takes place through an SN barrier, then this is the orthodox approximation specified below and σ_t becomes a function s_t (see below). The modern FE literature often makes the elementary approximation of taking $s_t = 1$, once Forbes [126] shows that $s_t \approx 0.95$. But, as it was shown by Forbes [123] if s_t is not considered the FN plot shows non-linearity therefore directly affecting the estimate of the emission area.

For many years, the only simple test for consistency of FE data with theory has been the qualitative one of whether an experimental FN plot is effectively straight. However, this criterion is not appropriate because many nonorthodox emission data may have a sufficient linear dependency in the FN plot.

4.4 The Orthodox Emission Hypothesis

The orthodox emission hypothesis is a set of physical and mathematical assumptions, proposed by Forbes [126], that permit well-specified analysis of measured current-voltage data related to CFE.

Real physical emission situations are never exactly orthodox, but some real situations are expected to be very nearly orthodox. In particular, emission from a stably mounted, metal, emitter of moderate-to-large apex radius (larger than $10nm$), with a good conducting path to the high-voltage supply, and emitting under stable vacuum conditions, is expected to be very nearly orthodox. Some other emitters complications can occur in real emission situations, but also may be disregarded, in some appropriate conditions, such as voltage drop in the measuring circuit; leakage currents; patch fields; field-emitted vacuum space charge; current-induced changes in emitter temperature; field penetration and band-bending; strong field fall-off; quantum confinement associated with small-apex-radius emitters [128]; and field-related changes in emitter geometry or emission area or local work function.

Such assumptions, that involve the voltage difference between the emitting regions and a surrounding counter-electrode (all parts of which are at the same voltage) can be treated as uniform across the emitting surface and equal to the measured voltage V_m; the measured current i_m can be treated as equal to the device current i_d, and as controlled solely by CFE at the emitter/vacuum interface; emission can be treated as if it involves deep tunnelling through an SN barrier, with the device current i_d described by a related FN-type equation in which the only quantities that depend (directly or indirectly) on the measured voltage V_m are the independent variable in the equation and the barrier-form correction factor; and the emitter local work

function ϕ is constant (and constant across the emitting surface), and has its assumed value.

Because of theses assumptions the correction physical parameters, such as λ_c, A_F and consequently α_F can all be treated as constants.

Forbes [126] has realized that from 1960 to 1990, nearly all literature analyses of measured CFE current-voltage data, in practice, assumed the orthodox emission hypothesis. However, as noted earlier, if emission is not physically orthodox, then orthodox data-analysis methods may generate spurious values for extracted physical parameters.

Based on the previous assumptions, Forbes has calculated [126], for any given emitter temperature a range of reasonable f values. For that, lets write the Eq. 4.55 as function of $f_c = F_c/F_R$, such that,

$$J_{kc} = \theta f_c^2 \exp\left(-\nu(f_c)\eta/F_c\right) \tag{4.64}$$

with the slope of an FN plot of type $ln[J_{kc}] \times f_c^{-1}$ being

$$S_{f_c} = -\eta s(f_c) \tag{4.65}$$

where $s(f_c)$ is the function (expressed here as a function of f_c) that is the slope correction function for the SN barrier[116]. The called work-function-dependent parameters $\eta(\phi)$ and $\theta(\phi)$ can be defined by

$$\eta(\phi) \equiv \frac{b\phi^{3/2}}{F_R} = bc^2\phi^{-1/2} \tag{4.66}$$

and

$$\theta(\phi) \equiv a\phi^{-1}F_R^2 = ac^{-4}\phi^3 \tag{4.67}$$

The values of $\eta(\phi)$ and $\theta(\phi)$ are shown in table 4.1

With the orthodox emission hypothesis, all sensible independent variables are linearly related to each other. Then, if a given dataset of a LAFE is plotted as function of F^{-1} rather than f_c^{-1}, then the slopes of the two plots are related by

$$S_F = S_{f_c}\frac{d(f_c^{-1})}{d(F^{-1})} = S_{f_c}F_R \tag{4.68}$$

As $F_R = F_c/f_c$ and Eq. 4.65,

$$S_{F_c} = -\eta s(f_c)\frac{F_c}{f_c} \tag{4.69}$$

This applies to a specific field F_t at which the tangent to the theoretically predicted plot is parallel to the fitted line with slope S^{fit}, so,

$$S^{fit} = -\eta s_t \frac{F_t}{f_t} \tag{4.70}$$

where $s_t \equiv s(f_t)$. Therefore, finally one is able to extract f^{extr} that relates to the experimental value $(F^{-1})^{expt}$ is

$$f^{extr} = \frac{-s_t\eta}{S^{fit}(F^{-1})^{expt}} \tag{4.71}$$

At sufficiently low f^{extr} values, owing to signal-to-noise issues in measuring instruments, the resulting emission currents may be too low to be measured. At sufficiently high f^{extr} values, the local current density may (for many emitter materials) be high enough to cause significant emitter heating, and consequent emitter failure (or, alternatively, be high enough to induce vacuum breakdown and emitter failure by some other mechanism). Table 4.1 shows the parameters F_R, η and θ for an SN barrier of zero-field height ϕ, and the corresponding f^{extr} values that set the 'apparently reasonable' range $f_{low} \leq f^{extr} \leq f_{up}$, and the 'clearly unreasonable' ranges $f^{extr} < f_{lb}$ and $f^{extr} > f_{ub}$.

ϕ (eV)	F_R (Vnm^{-1})	η	θ (Am^{-2})	f_{lb}	f_{low}	f_{up}	f_{ub}
4.5	14.06	4.3989	6.77×10^{13}	0.10	0.15	0.45	0.75
4.0	11.11	4.9181	4.76×10^{13}	0.105	0.16	0.48	0.79
3.5	8.51	5.2577	3.19×10^{13}	0.11	0.17	0.51	0.85
3.0	6.25	5.6790	2.01×10^{13}	0.12	0.18	0.54	0.91

Table 4.1: The dependence of F_R, η, θ and f values on work function ϕ[126], considered in this thesis.

The 'apparently reasonable' and 'clearly unreasonably' f's range shows in the table 4.1 was defined by Forbes [126] based on mainly by the experiments carried out in the 1925-1975 period. This because the emitters corresponding most closely to the physical assumptions of the orthodox emission hypothesis are the traditional ones, metal, single-tip field emitters

of relatively large apex radius, used in arrangements with a low-resistance path to the high-voltage supply. This means that one can appeal to the large body of experimental work in such mentioned period.

Chapter 5

Large-area field emitters: the dependence between area of emission and the applied field

With a large-area field electron emitter, the area of emission is expected to be dependent of the applied field. One possible explanation for this behavior is the statistical distribution of the local field enhancement factors, as a consequence of an irregular surface's morphology of the LAFE. In this section, we present a simple and more general theory for extracting the scaled barrier field, f, by considering the dependence of the formal area of emission of conducting LAFEs with an applied field. In our model, the local FEF of LAFE sites are exponentially distributed, which is consistent with thin film electron emitters. As a byproduct of technological relevance, our results show that general effective f values extracted from linear Fowler-Nordheim (FN) plots are outside of the "experimentally reasonable" range of values for physically orthodox emission, when the area of emission varies significantly with the applied field. Thus, a more general criterion for detecting and interpreting nonorthodox field emission is proposed and can be applied to any distribution of local FEFs in conducting LAFEs.

This chapter is based on reference [27]:

de Assis, T. A. and de Castro, C. P., *Extracting scaled barrier field from experiments with conducting large-area field emitters: Considerations by inclusion of the dependence between area of emission and the applied field*, Journal of Vacuum Science & Technology B, **35**, 052201 (2017).

5.1 The dependency of the formal area of emission on the applied field and LAFE model

A LAFE can be treated as an array of emitters or emission sites, each with its own characteristics, that stand upright on a flat plate [129]. A more realistic situation that includes the nonuniformity of the LAFE geometry requires a distribution of local FEFs [130, 131, 132]. Chemically etched tungsten tips or Spindt-like emitters often have poor tip-to-tip reproducibility [132]. To incorporate this effect, de Assis introduced a dimensionless LAFE parameter ω_0 defined by [26, 29]

$$\omega_0 \equiv 1 + \frac{\partial \ln(\alpha_f)}{\partial \ln(J_{kC})}. \tag{5.1}$$

We interpret this parameter as an indirect measure of the dependence of the LAFE formal area A_f on F_M. If there is no field dependence, then $\omega_0 = 1$, and a linear dependence between J_M and J_{kC} is expected [see Eq. (4.54)]. Recently, for a Gaussian distribution of local FEFs [29] with an appropriate range of applied electrostatic fields within the conducting materials (i.e., $1V/\mu m \leq F_M \leq 10V/\mu m$), J_M was shown to vary as $J_M \sim (J_{kC})^{\omega_0}$. This power law dependence can be interpreted by assuming that the field emission predominantly originates from sites with characteristic FEFs γ_C and $\omega_0^{-1}\gamma_C$, $\omega_0 > 1$ [26, 29]. Then, parameter ω_0 provides information regarding the characteristic FEF of the n-th site of the LAFE that contributes significantly to the field emission beyond site "C" with the maximum FEF for regimes with a high applied electrostatic field.

Assuming that two sites in the LAFE predominantly participate in the emission within the corresponding range of the applied electric field, the macroscopic emission current density, J_M,

can be calculated as follows:

$$J_M \approx \frac{\sum_{n=1}^{2} J_{kc}^n \sigma_f^n A_s^n}{A_M}, \tag{5.2}$$

where σ_f^n is the formal area efficiency, A_s^n is the site area (i.e., the "footprint" area associated with the individual emitter or emission site), and J_{kc}^n is the kernel characteristic current density of the n-th site of the LAFE. If n_s is the number of sites of the LAFE and $A_s^1 = A_s^2 = ... = A_s^n$, then the macroscopic area of the LAFE can be written as $A_M = n_s A_s^1 = n_s A_s^2$.

Considering that $\gamma^1 = \gamma_C$ and $\gamma^2 = r\gamma^1$ when $0 < r < 1$ and that the emission from all sites can be treated as deep tunneling through an SN barrier, the kernel characteristic current densities of sites 1 and 2 are respectively given as follows:

$$J_{kC}^1 \approx a\phi^{-1} \exp(\eta) F_R^{\eta/6} (\gamma_C F_M)^{\kappa} \exp\left[-b\phi^{3/2}/(\gamma_C F_M)\right], \tag{5.3}$$

and

$$J_{kC}^2 \approx a\phi^{-1} \exp(\eta) F_R^{\eta/6} r^{\kappa} (\gamma_C F_M)^{\kappa} \exp\left[-b\phi^{3/2}/(\gamma_C F_M)\right]^{1/r}, \tag{5.4}$$

where $\kappa \equiv 2 - \eta/6$. From Eq.(5.2), it is possible to write:

$$J_M \approx \frac{1}{n_s} \left\{ \sigma_f^1 + \sigma_f^2 \frac{J_{kC}^2}{J_{kC}^1} \right\} J_{kC}^1. \tag{5.5}$$

By inserting Eq.(5.3) into Eq.(5.4), the ratio J_{kC}^2/J_{kC}^1 is given by:

$$\frac{J_{kC}^2}{J_{kC}^1} = \frac{a\phi^{-1} \exp(\eta) F_R^{\eta/6} (\gamma_C F_M)^{\kappa}}{a^{1/r} \phi^{-1/r} \exp(\eta/r) F_R^{\eta/6r} (\gamma_C F_M)^{\kappa/r}} \left(J_{kC}^1\right)^{1/r-1}. \tag{5.6}$$

At a high applied field limit and considering $\sigma_f^2 >> \sigma_f^1$, Eq. (5.5) can be approximated by:

$$J_M \approx \frac{1}{n_s} \left\{ \sigma_f^2 \frac{J_{kC}^2}{J_{kC}^1} \right\} J_{kC}^1. \tag{5.7}$$

The contribution to the macroscopic current density under the approximation given by Eq. (5.7) clearly originates from the sites with FEF γ^2. By using Eq. (5.6) in Eq.(5.7), this conclusion

is equivalent to:

$$J_M \approx \frac{J_{M0}}{(J_{kC0})^{1/r}} \left(J_{kC}^1\right)^{1/r}, \tag{5.8}$$

where J_{M0} and J_{kC} are given by:

$$J_{M0} = n_s^{-1}\sigma_f^2 a r^\kappa \phi^{-1} \exp(\eta) F_R^{\eta/6} (\gamma_C F_M)^\kappa, \tag{5.9}$$

and

$$(J_{kC0})^{1/r} = a^{1/r}\phi^{-1/r} \exp(\eta/r) F_R^{\eta/6r} (\gamma_C F_M)^{\kappa/r}. \tag{5.10}$$

Then, by using the definition of $\omega_0 \equiv d\ln(J_M)/d\ln(J_{kC}^1)$, we identify $\omega_0 = r^{-1}$. Clearly, in the limit of a high applied field [i.e., when the approximation given by Eq. (5.7) is valid], $\omega_0 > 1$.

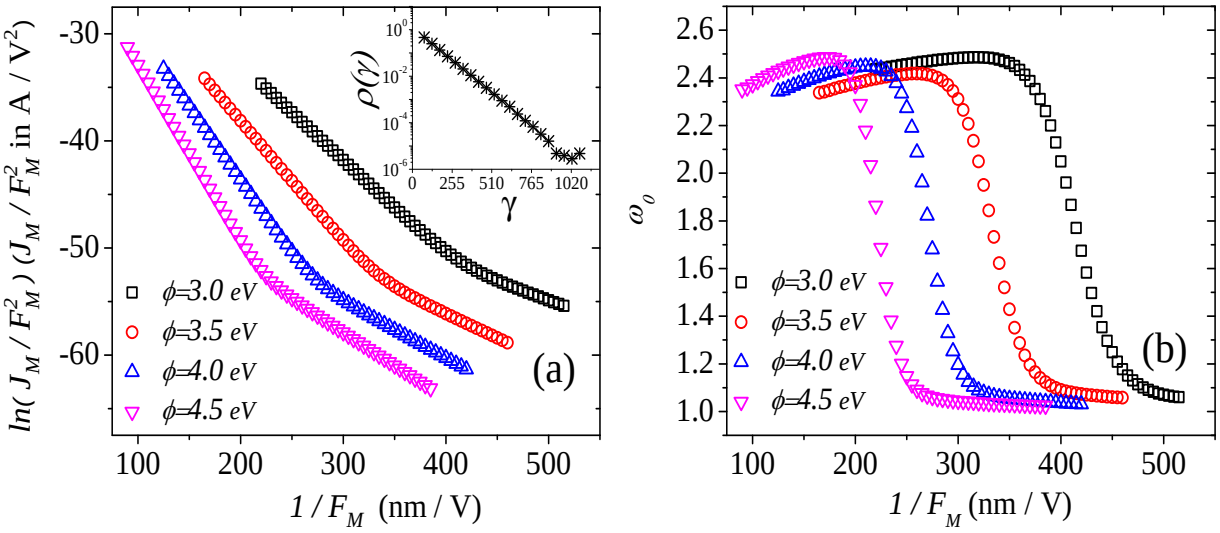

Figure 5.1: (Color online) (a) Ordinary FN plots simulated for the different local work functions considering that the local FEF sites in the LAFE are exponentially distributed, i.e., $\rho(\gamma) = \exp(-\xi\gamma)$ with $\xi = 1/80$, and $\gamma \in [50, 1100]$, as shown in the inset. The macroscopic current density was computed using the ratio between the integration of the site current [see Eq. (5.11)] over the entire LAFE and the macroscopic area (or "footprint") of the LAFE, A_M. (b) Effective ω_0 values were evaluated by using Eqs. (5.2) and (5.1) as a function of $1/F_M$, for several local work functions.

In this work, we assume that the LAFEs have an exponential distribution of site-characteristic FEFs, i.e., $\rho(\gamma) = \exp(-\xi\gamma)$, where ξ is the characteristic decay rate. This distribution is consistent with previous experimental works that have found, using scanning anode field emission microscopy, exponential distributions of FEFs in carbon-based thin film electron emitters [131].

This type of distribution has also been found in theoretical works that considered the tails of the distributions obtained by assuming that the surface geometry of the LAFE was characterized by a Hurst exponent [26]. Moreover, in our simulations, we used $\xi = 1/80$ and $\gamma \in [50, 1100]$. This value of ξ ensures that the n-*th* LAFE site has a high probability of having a characteristic FEF $\gamma_n < \gamma_C$. The values of γ are consistent with other LAFE-based technologies [16]. The emission current associated with an individual n-th site has been obtained as follows. The local emission current density, J, is integrated over the area associated with the emission site A_s (i.e., the "footprint" associated with the individual emitter or emission site), and the result is written as follows:

$$i_s = \int J dA = \sigma_f A_s J_{kn}, \tag{5.11}$$

where the formal site efficiency, σ_f, introduced recently by Forbes and de Assis [133], corresponds to the ratio of A_f/A_s, and J_{kn} is the kernel characteristic current density for the n-th site. For the sake of simplicity, we consider that the footprint areas of all sites are the same. Furthermore, σ_f is expected to be anti-correlated with the local site FEF, γ_n. This aspect is interesting because σ_f may produce real nonlinearities in the FN plots, similarly to current voltage characteristics discussed in the experimental work of Lauritsen [134], observed also in Molybdenum Spindt field emission arrays [135] and theoretically treated in Refs. [136, 137].

5.2 Results and generalization for scaled barrier field extraction

In our simulations, we generate LAFEs formed with 10^6 sites with $\sigma_f = 10^{-14}$ for $\gamma_n > 400$, otherwise $\sigma_f = 10^{-6}$. Fig. 5.1(a) shows the ordinary FN plot of type $\ln(J_M/F_M^2)$ vs $1/F_M$, where J_M is computed using the ratio between the sum of Eq. (5.11) over all LAFE sites and the macroscopic area A_M. To compute J_{kn}, we used the Schottky-Nordheim (SN) barrier for the zero-field height $\phi = 3.0, 3.5, 4.0$ and 4.5 eV [see Eq. (2.2) of Ref.[126]]. Two regions with nearly constant and different slopes, which is characteristic of a kinked-FN plot, were observed. The theoretical FN plot stops at the value of $1/F_R$, where F_R corresponds to the reference

field necessary to reduce an SN barrier to zero. For $\phi = 3.0, 3.5, 4.0$ and 4.5eV, the F_R values are $6.25, 8.51, 11.11$, and 14.06 V/nm, respectively [126]. However, the experimental plot is expected to stop before $1/F_M$ to be reduced to $1/F_R$ because the emitter will melt or explode [125]. Thus, we consider a more realistic situation in which, for a given LAFE, the maximum local electric field of a site cannot surpass the values of $F_n = \gamma_n F_M = 0.8F_R$. This condition defines the higher limit values to F_M in the simulations of the FN plots. We stress that the conditions imposed here enable one to consider a more simple picture where vacuum voltage breakdown effects, which may be enhanced at high current densities regime [138, 139], can be discarded.

In the inset of Fig. 5.1(a), the exponential distribution of $\rho(\gamma)$ considered in this work is shown. From Eqs. (5.2) and (5.1), it is possible to compute the effective ω_0 as a function of $1/F_M$ for several local work functions. The results are shown in Fig. 5.1(b). In the lower F_M regime, ω_0 is close to unity, and A_f changes only slightly. However, for high applied fields, ω_0 is clearly higher than unity, indicating that $\frac{\partial \ln(\alpha_f)}{\partial \ln(J_{kC})} > 0$. In this regime, A_f clearly changes with F_M. Despite this, we observe a region of the FN plot exhibiting a nearly linear behavior.

For this range of the applied field, the sites of LAFE with $\gamma_n = \omega_0^{-1}\gamma_C$ dominates the emission. These features lead to the following questions: for high effective ω_0 values, is the orthodox emission expected to fail? Can γ_C be estimated in a more reliable way from a nearly linear FN plot, even for $\omega_0 > 1$? To address these questions, we propose a generalized method for extraction of the scaled barrier field for situations where $\omega_0 > 1$. The orthodoxy test was developed by Forbes [126] by considering A_f constant, as pointed previously. In our case, this generalization is particularly useful to characterize conducting LAFEs as thin film emitters, in which the formal area is expected to increase as the applied field increases.

From the n-th site of the LAFE, where $\gamma_n = \omega_0^{-1}\gamma_C$, it is possible to define the corresponding kernel characteristic current density as follows:

$$J_{kn} = \theta\omega_0^{-2} f_C^2 \exp\left\{-\nu(f_C/\omega_0)\eta\omega_0/f_C\right\}, \tag{5.12}$$

where θ and η are work-function-dependent parameters defined by $\theta \equiv ac^{-4}\phi^3$ and $\eta \equiv bc^2\phi^{-1/2}$, where a [$\approx 1.54 \times 10^{-6}$A (eV V^{-2})] and b[$\approx$ 6.83 eV$^{3/2}$ (V nm^{-1})] are the first and second FN constants, respectively, and c[$\approx$ 1.199 eV (V nm^{-1})$^{-1/2}$] is the Schottky constant. In addition, f_C is the scaled barrier field corresponding to the barrier field F_C, which is given by $f_C \equiv F_C/F_R = c^2\phi^{-2}F_C$ for ϕ [126]. The definition related to Eq. (5.12) is justified by the anti-correlation imposed between σ_f and γ_n in the following manner: when σ_f is associated with FEF site γ_n ($\gamma_n < \gamma_C$) and is sufficiently high compared with σ_f associated with γ_C, the dominant field emission comes from the sites with FEF γ_n in the high F_M regime. This explains the differences in the slopes of the FN plots shown in Fig. 5.1(a).

For convenience, we use $\nu(f_C/\omega_0) \equiv \nu_{\omega_0}$ for the simple and accurate approximation (see Ref.[120]) of the SN barrier [120, 116]

$$\nu_{\omega_0} = 1 - f_C/\omega_0 + \frac{1}{6}(f_C/\omega_0)\ln\left(\frac{f_C}{\omega_0}\right). \tag{5.13}$$

Then, for the variables of the FN plot, we write

$$\ln\left\{\frac{J_{kn}}{f_C^2}\right\} = \ln(\theta) - 2\ln(\omega_0) - \nu(f_C/\omega_0)\eta\omega_0/f_C. \tag{5.14}$$

From Eq. (5.14), we obtain the slope of the FN plot of type [$\ln\{J_{kn}/f^2\}$ vs f^{-1}], S_f. Hence, for simplicity, $f_C \equiv f$, S_f is presented as follows:

$$S_f = -\frac{2}{\omega_0}u - \eta\left[s_{\omega_0}\omega_0 + \nu_{\omega_0}f^{-1}u\right], \tag{5.15}$$

where the functions u and s_{ω_0} are defined as:

$$u \equiv \frac{\partial\omega_0}{\partial\{f^{-1}\}}, \tag{5.16}$$

and

$$s_{\omega_0} \equiv \frac{\partial\{\nu_{\omega_0}f^{-1}\}}{\partial\{f^{-1}\}}. \tag{5.17}$$

Fig.s 5.2(a), (b) and (c) show the dependence of ν_{ω_0}, u and s_{ω_0} on F_M computed using Eqs.

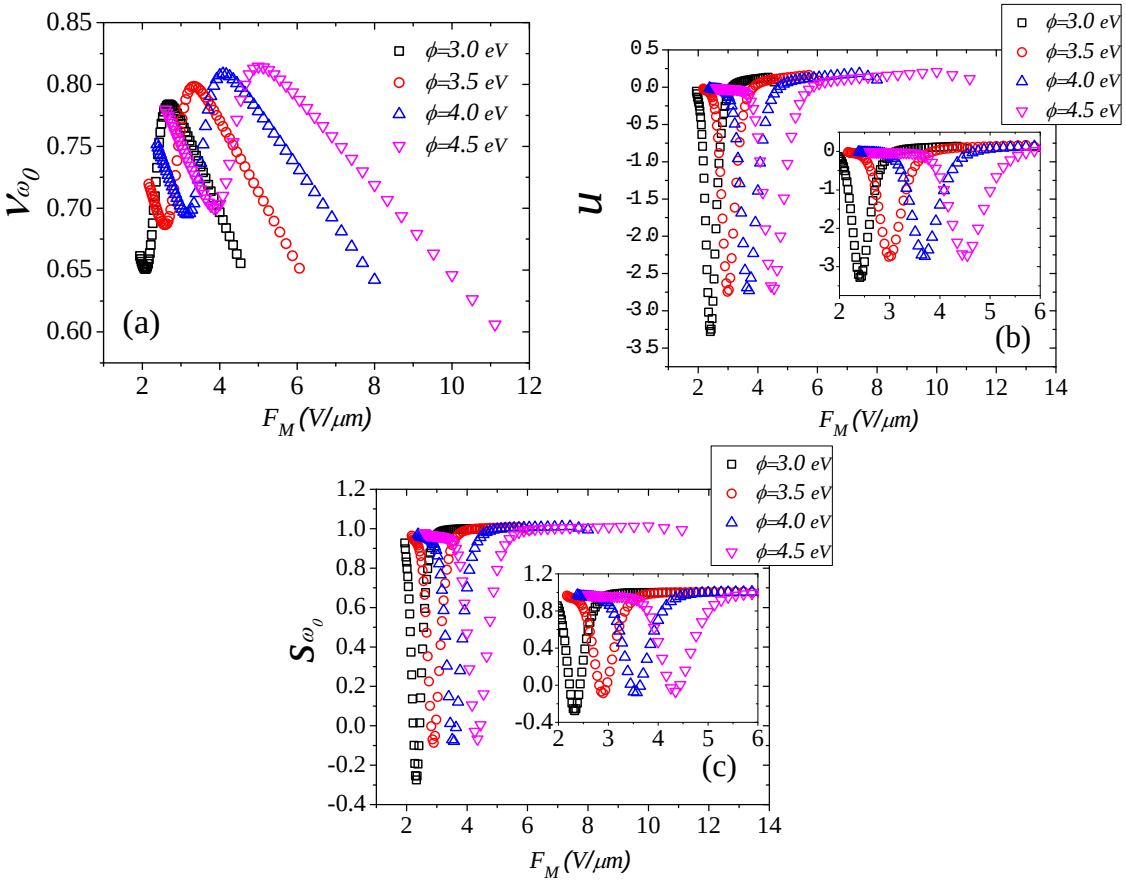

Figure 5.2: (Color online) Functions (a) ν_{ω_0}, (b) u and (c) s_{ω_0} defined by Eqs. (5.13), (5.16) and (5.17), respectively, as a function of the applied macroscopic field, F_M, for several local work functions. The insets in (b) and (c) show a magnification of the main panel data for 2 V/μm $\leq F_M \leq$ 6 V/μm.

(5.13), (5.16) and (5.17), respectively. The results were computed using the FN plots and ω_0 presented in Figs. 5.1(a) and (b). Interestingly, the function ν_{ω_0} presents minimum and maximum values that increase as the local work function increases. This justifies the subtler nonlinear behavior of the FN plot for the lower values of the work functions. Additionally, the functions u and s_{ω_0} present a clear plateau for all work functions considered in this study, whereas the corresponding FN plots have an approximately linear behavior. Interestingly, in the quasilinear regions of the FN plots, $u \approx 0$, suggesting that ω_0 varies slowly with f^{-1}. In these circumstances, Eq. (5.15) can be approximated as follows:

$$S_f \approx -\eta s_{\omega_0} \omega_0. \tag{5.18}$$

If S_F is an effective slope of an ordinary FN plot of type $\ln(J/F^2)$ vs $1/F$ and, given the linear

dependence between F and f, $S_F = S_f \partial(f^{-1})/\partial(F^{-1})$. By using approximation given by Eq. (5.18), it is possible to obtain

$$f_{\omega_0} \approx -\frac{\eta s_{\omega_0} \omega_0}{S_F\left(\frac{1}{F}\right)}. \tag{5.19}$$

The approximation given by Eq. (5.19) is a generalization for extraction of the scaled barrier field, including the effects of the variation of A_f with F_M. Fig. 5.3 shows the results for f_{ω_0} after using Eq. (5.19) and the data from Fig. 5.1 for the high field regime ($\omega_0 > 1$) as a function of the applied electric field. The data used correspond to a nearly linear FN plot in which $u \approx 0$. As we can see, f_{ω_0} is outside of the range for "apparently reasonable" orthodox emission [126], which is consistent with the dependence between A_f and F_M. In contrast, by using the scaled barrier field $f_{orth} \approx 0.95\eta/[S_F\,(1/F)]$ obtained from the orthodox field emission hypothesis [126], the effective f_{orth} values fall approximately within the range of orthodox emission. These results suggest that a more general criterion for detecting nonorthodox field emission is enabled by using Eq. (5.19) in high applied field regime.

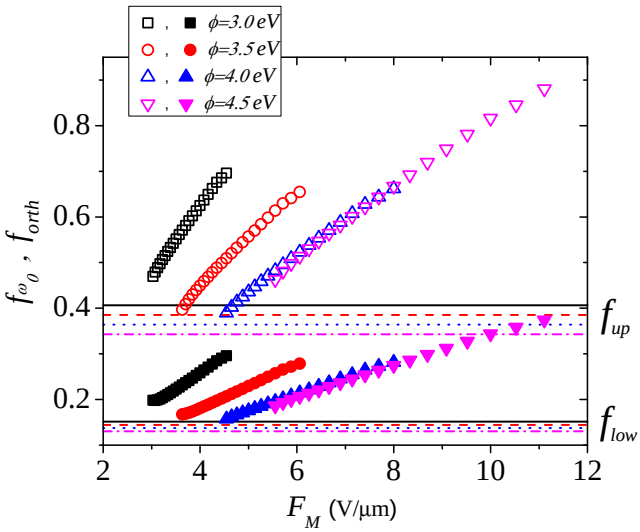

Figure 5.3: (Color online) Generalized scaled barrier field, f_{ω_0} (hollow symbols), calculated using Eq.(5.19) and data from Fig. 5.1 as a function of the applied electric field for various work functions. The results using f_{orth} (full symbols) from orthodox emission hypothesis are also shown. The limits of f_{low} and f_{up} for "apparently reasonable" orthodox emission [126] for all work functions considered in this study are shown.

5.3 Discussion of the discrepancies between the slope characterization parameter, β^{FN}, and the approximated FEF, γ_C^{aprox}, extracted from simulated FN plot data at high applied field regime

Now, we address how γ_C can be estimated in a more reliable way from a nearly linear FN plot, for $\omega_0 > 1$. From a $(J_M - F_M)$-type FN plot, it is possible to define the elementary slope characterization parameter, β^{FN} (also called the "apparent FEF"). This quantity, which is used by experimentalists to estimate γ_C, is given by:

$$\beta^{FN} \equiv -b\phi^{3/2}/S_F, \tag{5.20}$$

where S_F is the extracted slope from an experimental FN plot. If we assume that $J_M \sim (J_{kC})^{\omega_0}$, ω_0 is approximately constant in a given range of F_M [i.e., $u \approx 0$ - see Eq. (5.16)], and s_t is the fitting value of the slope-correction function, s for the SN barrier (for an FN plot), then an approximation of γ_C^{aprx} for the true FEF γ_C can be derived from:

$$\gamma_C^{aprx} = -\omega_0 s_t b\phi^{3/2}/S_F = \omega_0 s_t \beta^{FN}. \tag{5.21}$$

Table 5.1 summarizes the values of γ_C extracted from the distribution $\rho(\gamma)$, and β^{FN} and γ_C^{aprx} extracted from the FN plots shown in Fig.5.1 (a) considering the linear behavior in the limit of a high applied field. In fact, the exact value of s_t is always unknown, but a good approximation for metals is 0.95 [126]. As we can see, γ_C^{aprx} is a good estimation of γ_C (with deviations no higher than 12%) for all work functions used. This result supports that the parameter ω_0 should be considered experimentally to correctly interpret the FEFs extracted from a conducting LAFE when the following conditions are met: (i) the formal area is expected to change with the applied field and (ii) the effects of the resistance in series in the field emission device are discarded.

Some recent experiments have observed a nonlinear behavior in the corresponding current-voltage characteristics, similarly to that presented in Fig.5.1(a) (see for instance Refs.[140, 141]). In particular, Popov *et al.* [142] have implemented experimental methods for determining emission area parameters (e.g. formal area A_f) from FN plots using several multi-tip emitters based on CNT and graphene. In addition, by experimental measurements of the macroscopic emitted current, i_m, the characteristic current density, J_{kC}, may be estimated. This probably should be the first step to an indirect measuring of the ω_0 parameter defined in Eq.(5.1). Of course, careful interpretation is necessary since all the theory constructed in this work assumes that the characteristic point "C" in the LAFE is formally taken at the apex of the emitter with the highest local apex FEF.

ϕ (eV)	$S_F(V/nm)$	β^{FN}	γ_C	γ_C^{aprx}
3.0	-0.0891(2)	398.3	1065.7	983.5
3.5	-0.112(6)	397.2	1057.1	949.5
4.0	-0.1378(3)	396.5	1078.2	955.7
4.5	-0.1651(5)	394.8	1091.7	963.4

Table 5.1: Values of γ_C extracted from the distribution $\rho(\gamma)$, β^{FN}, γ_C^{aprx} and the slopes S_F extracted from the FN plots shown in Fig.5.1 (a). The results are presented for the linear region of the FN plot in the limit of a high applied field, for various work functions.

5.4 Conclusions

In this work, we consider the dependence of the formal area of emission on the applied field to provide a more general method for extraction of the scaled barrier field from current-voltage characteristics. This makes the link between theory of CFE and experiments more strong for LAFE technologies purposes. The effects of the resistance in series in the field emission device were not considered in this work. Even under these circumstances, our results suggest that nonreliable conclusions may appear if the values of the scaled barrier field were extracted applying orthodox equation in real nonorthodox field emission data. As a consequence, if we only observe linearity in the FN plots in the high applied field regime and use the elementary slope characterization parameter $\beta^{FN} \equiv -b\phi^{3/2}/S_F$, we may observe a larger discrepancy in

this quantity compared with real value of the maximum FEF of the LAFE γ_C. This aspect leads to the following conclusion: even when the f values extracted experimentally using the orthodox equation fall approximately within the range of orthodox emission, extracting β^{FN} may not be conclusive for a properly characterization of LAFE. Therefore, evaluating the ω_0-parameter, which provides information about the dependence of the formal area of emission on the applied field, is necessary during LAFE measurements.

Finally, if ω_0 is near unity, the effect of the relationship between A_f and F_M is not sufficiently large to fail the orthodoxy test, once $f_{\omega_0} \approx f_{orth}$. Then, the merit of our results is identifying that a nearly linear FN plot may hide high values of ω_0. This allows that a nonorthodox emission may be masked by the use of the scaled barrier field expression derived from the orthodox hypothesis. Then, ω_0 should be measured before deciding which expression of the scaled barrier field provides a more careful interpretation of experimental field emission data. Importantly, this parameter enables a more precise extraction of γ_C, which is a necessary parameter for determining if a device is suitable to operate at lower applied field regimes.

Chapter 6

Degradation of a large area field emitter: from saturation in Fowler-Nordheim plots to unorthodox field electron emission

We present a simple model that is able to demonstrate that degradation on the morphology of a conducting Large Area Field Emitter (LAFE) may cause a kinked behavior formed by two clear linear regimes before saturation on the corresponding ordinary Fowler-Nordheim (FN) plot. Importantly, we show that in the nearly linear regime observed, even after the degradation has been started, spurious values of the slope characterization parameter can be achieved. This feature is a strong evidence that the changing in the morphology of the LAFE during the increasing of the applied field can lead to an unorthodox field emission. Our results show that the effective scaled barrier field extracted from the simulated FN plot in our model is consistent with those found for Au posts on flexible graphene film, probably justifying the general mechanism (i.e., field dependent changes in emitter's geometry) behind unorthodox field emission observed on current-voltage characteristics of that experiment. Finally, our results suggest that the transition from the latter nearly linear behavior to saturation regime on FN

plot contains a signature of the morphology of a LAFE before degradation.

6.1 Introduction

Fowler-Nordheim (FN) plot saturation has been justified by several physical phenomenon, such as internal resistance of the emitters, which lead to the voltage loss (voltage drop)[143, 144, 145, 129], field penetration [146], field-emitted vacuum space charge[147], the transition from thermionic to field emission[148], and also a voltage-divider effect, due to measurement-circuit resistance [28, 129]. An important limiting factor for various applications, which includes electron sources, is the vacuum arcing which is known appears after intense field electron emission (FE). A commom hypothesis behind this phenomenon is that intense FE leads to high local electron current densities producing Nottingham heating [149, 150] which leads to local temperatures close to the melting point of the emitter with evaporation of neutral atoms [151, 152, 153]. This may occur in single [153] or large-area field emitters (LAFEs) [154] implying in a change of the related morphology [152, 155]. Actually, the phenomena behind the degradation of field emitters are not completely understood at present, and several factors play an important role. For instance, the shape of an emitter may be changed by electrostatic deflection or mechanical stresses leading to a decreasing of the local field enhancement factor (FEF). Field evaporation of the emitter may be sometimes the mainly cause of decreasing the local FEF [156]. Failures during field emission at or near the substrate-emitter contact has been reported for individual multiwall carbon nanotubes [157]. For a film emitter, the degradation may be abrupt and sometimes gradual ocurring during initial current-voltage characteristic tests as well as at constant applied field in long periods [155]. Some works considering multi-tip emitters reported that the decrease in FEF associated with the degradation may be due to the failure of individual emitter [155, 156], which can occur already for currents of few hundreds of nanoamperes per emitter.

The degradation of a field emitter is expected to be reflected on the corresponding current-voltage characteristics. As a consequence, a non orthodox field emission is expected to occurs

[126]. For instance, field emission measurements of Au posts grown on exible graphene film by electrodeposition method [31] confirmed that the extracted scaled field barrier was in a range "clearly unreasonable" as compered with that expected for orthodox field emission [158]. This result, still not fully understood, has as a possible explanation the field-dependent changes in emitter's geometry [126]. Cahay and collaborators [159] reported different behaviors in the FN plots from field emission measurements with carbon nanotube fibers (CNFs), as the values of the fiber tip to anode spacing decreased. Interestingly, the corresponding FN plots presented saturation features. Their results suggested that some of the sharper features contributing to FE at the large gap distance were destroyed at largest applied fields, leaving CNFs with lower FEFs and thereby causing an increase in the threshold for FE. Moreover, this destruction has been stated to arise from a combination of self-heating effects and ion back bombardment [155]. Also, a multiscale model of FE from CNFs has been developed [162], which takes into account Joule heating within the fiber and the Nottingham effect at the tip of the individual carbon nanotubes (CNTs) in the array located at the fiber tip [162, 160].

Motivated by aforementioned results, in this paper we investigate theoretically, by using Monte Carlo simulations, how degradation of LAFE affects the corresponding ordinary FN plots and how this degradation is connected with its saturation. Importantly, we show that the degradation may cause a clear nearly linear regime on FN plot before saturation, with smaller slope as compared with one of the linear regime before the degradation has started. Our results suggest that degradation in LAFE affects directly the characteristic FEF of the LAFE, γ_C, as a consequence of the changing in LAFE's morphology. Therefore, this linear regime may mask the degradation and confirm that spurious information of the slope characterization parameter may be extracted from the FN plot, connecting changing of the morphology of a LAFE with the non orthodox field emission.

The section is organized as follows. Section 6.2 describes the method to model the degradation of the LAFEs used in this work. In section 6.3, we discuss the results and section 6.4 presents our conclusions.

6.2 Method

In our model, a n-th individual site (emitter) of the LAFE is assumed to be spaced in such way the electrostatic effects (shielding) between the emitters can be neglected. Furthermore, if the local work function along the surface of the emitter is assumed to be constant, we associate a local characteristic FEF, $\gamma_n = F_n/F_M$, most likely situated at the apex of the n-th emitter if the morphology of the site's surface is consistent with a classical smooth surface. Considering cold field electron emission (CFE), F_n corresponds to the field defined in the emitters electrical surface, which determines the barrier through which the field-emitted electrons tunnel.

This characterization parameter, which can be experimentally extracted from current-voltage characteristics from a LAFE [28, 29, 26] in the case of orthodox emission [126], is a measure of the sharpness of the system. For technological purposes, it has values ranging typically between 10^2 and 10^3. For generality of our results and technological reasons on cold field emission[30, 163, 16], the emitter and counter-electrode are assumed to be sufficient distant, such that γ_n become independent of this gap only depending on the geometry of the system. As showed by Bonard *et al.*[35], for large area emitters formed by multi-wall carbon nanotubes, only sites with the highest characteristic macroscopic FEFs contribute effectively to the emission current. Based on this, one defines the highest FEF of all sites of the LAFE as being the macroscopic characteristic FEF for the LAFE, γ_C. The characteristic FEF has technological importance because high γ_C-values may indicate an initialization of the field emission at sufficiently low applied electrostatic field (typically of the order or fraction of few V/μm [160]).

Since the seminal paper on CFE on metal surfaces by Fowler and Nordheim (FN)[164], several relevant corrections have been proposed improving the FN theory. Such corrections take into account important physical effects generating a more realistic description for field emission through Fowler-Nordheim-type (FN-type) equations[118, 124, 120, 165]. For conducting emitters with appropriate dimensions (i.e. radius of the emitter no less than 10nm[126]), and considering the emission described by deep tunneling through a Schottky-Nordheim (SN) barrier[121, 161] used in the Murphy-Good (MG) theory[167], a technically complete expression for the characteristic local emission current density, associated to the n-th site, J_n is written as

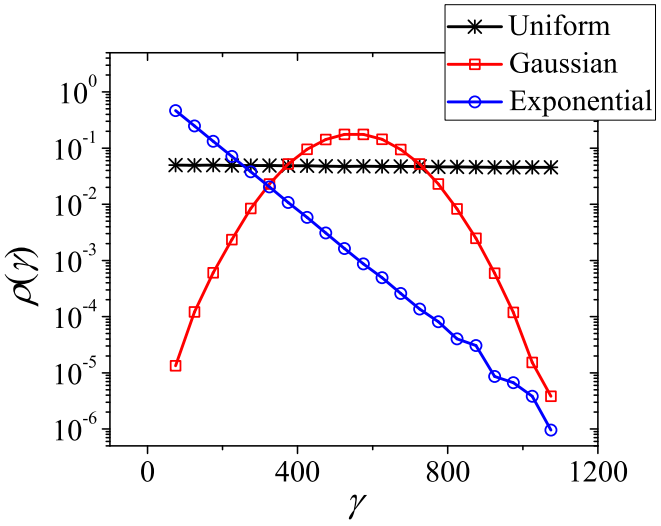

Figure 6.1: Exponential, uniform and Gaussian distributions of the characteristic FEFs of the sites ranging $50 \leq \gamma \leq 1100$. The distributions $\rho(\gamma)$ were simulated considering a LAFE formed by 10^6 sites.

follow,

$$J_n = \lambda_n J_{k,n}, \tag{6.1}$$

$$J_{k,n} = aF_n^2\phi^{-1}\exp\left(-\nu_{f_n} b\phi^{3/2}/F_n\right), \tag{6.2}$$

where $J_{k,n}$ is a characteristic kernel current density associated to a n-th site [126] and ν_{f_n} is the corresponding barrier-form correction factor for the SN barrier[120]. The local pre-exponential correction factor λ_n[126, 116] includes various effects known to influence the emission process, as correct integration over emitter electron states, the influence of emitter's temperature, the use of atomic level wave functions and band structure. Currently, the best guess is that λ_n lies in the range $0.005 < \lambda_n < 11$. In the present work, possible field dependence in λ_n is disregarded. In this case, our results do not depend qualitatively on what value is assumed for λ_n; for convenience we shall set $\lambda_n = 1$ in all simulations presented here. The first and second FN constants[30] are a=1.541434 $\times$ 10^{-6} $A\ eV\ V^{-2}$ and b=6.830890 $eV^{-3/2}\ V\ nm^{-1}$, respectively. Thus, the macroscopic current density J_M of a LAFE is the ratio between the sum over all the local site's current emitted i_n and the macroscopic emitters' footprint area, such that,

$$J_M = \frac{\sum_{n=1}^{N} i_n}{A_M} \quad , \qquad i_n = \sigma_n J_n A_s, \tag{6.3}$$

where N is the total of sites of the LAFE. In this work, we considered a LAFE formed by N=10^6 sites. A_s is the site's area, A_M is the whole macroscopic area of the LAFE and σ_n is the notional area efficiency [133], which we kept constant for every site and assumed a typical value $\sigma_n = 10^{-10}$ (see Ref.[18]).

For a barrier of zero-field height h, F_h is defined as the field necessary to reduce a tunneling barrier from its zero-field height h to zero. Therefore, as the SN barrier has $h = \phi$, $F_\phi = c^2\phi^{-2}$ (see Refs. [31] and [33]). By the physical meaning of F_ϕ, we simulated the mechanism of morphology degradation in our model as follows: (i) For a specific applied field, F_M, we define a maximum local field for the site being a fraction of the reference field, i.e., δF_ϕ, with $0 < \delta < 1$; (ii) As soon as a local field F_n exceeds δF_ϕ, a new value for F_n (smaller than δF_ϕ) is randomly selected. By this procedure, we were able to include in our simulation the effect of degradation of the LAFE due to high local electrostatic field and count the number of sites degraded. This procedure allows us to compute the fraction of degraded sites in the LAFE and it dependence with the applied field.

Based on experimental analyzes of FEF's distribution, via scanning anode field emission microscopy (SAFEM) [132, 7], we assume three different distributions of site-characteristic FEFs for the LAFE: an exponential distribution $\rho(\gamma) = \exp(-\zeta\gamma)$, where ζ is the characteristic decay, a Gaussian distribution and an uniform distribution, as shown in Fig.6.1. For exponential distribution, we have used $\zeta = 1/80$ (see Ref.[43]). The Gaussian distribution was truncated to ensure the range $\gamma \in [50, 1100]$, following the function $\rho(\gamma) = [A/(w\sqrt{\pi/2})]\exp[-2(\gamma-\bar{\gamma})^2/w^2]$, where $A \approx 5002$, $w \approx 222$ and $\bar{\gamma} \approx 550$.

6.3 Results and Discussion

As a consequence of the degradation of the LAFE, a saturation is observed in the ordinary FN plot, as shown in Fig.6.2. As we can see for an exponential distribution of the FEFs and $\delta = 0.4$, the saturation in the FN plot arises for different values of the work function. For smallest values of ϕ (i.e. for $\phi = 3.0eV$ and $3.5eV$), the effects of the degradation of the LAFE over the FN-plot

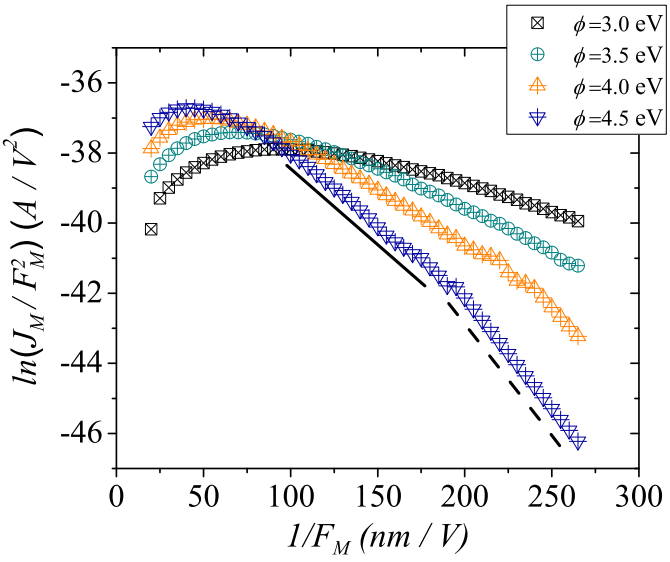

Figure 6.2: Fowler-Nordheim plot of a LAFE simulated with local FEFs exponentially distributed for $\delta = 0.4$, and different work functions ϕ. The full and dashed lines are guide to the eyes representing a kinked FN behavior.

initiate for lower values of F_M, as expected. Therefore, there is only one approximately linear region in the FN plot for these values of ϕ, in this specific range of external applied electric field, which corresponds to that similarly observed in low applied field for $\phi = 4.5eV$ (see Fig.6.2). Interestingly, as soon as F_M increases for $\phi = 4.5eV$, two nearly straight regions can be detected before the saturation in FN plot. For low F_M regime, the intensity of the F_M does not generate a local electric field in LAFE that surpasses $0.4F_\phi$ and then no degradation of the LAFE is expected. Consequently, the FN plot shows the linear behavior. For intermediate F_M-values, the degradation of the LAFE has already started generating such new nearly linear behavior with smaller slope as compared to the previous linear regime as shown in Fig.6.2. Finally, the saturation of the FN plot occurs in the limit of high values of F_M.

Next, we discuss that the behavior of the FN plot may reflect the signature of each initial distribution of FEFs before LAFE's degradation. In fact, the consequences of degradation of the initial LAFE's morphology may be observed as follows by the analysis of Fig.6.3. For uniform distribution of FEFs, a sudden saturation of the FN plot is observed, as compared with that observed for LAFEs with both Gaussian and exponential distribution of local FEFs. This feature is justified because the initial degradation of the LAFE with $\rho(\gamma)$ uniform covers a large number of sites that contribute for FE. In contrast, the transition from linear to saturation

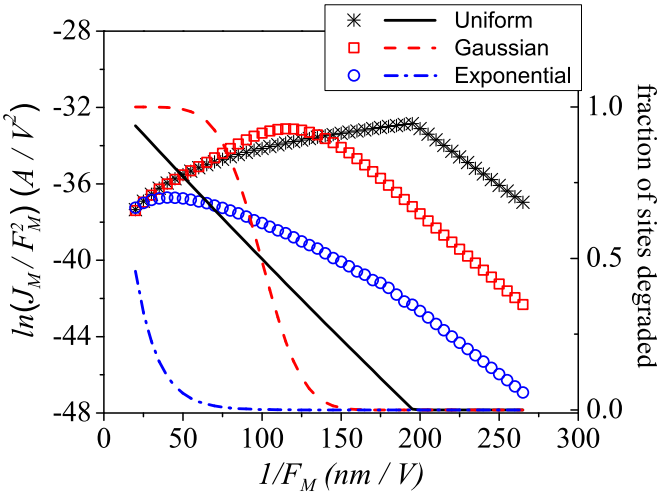

Figure 6.3: Ordinary FN plots for a LAFE simulated with different distributions of FEFs (dotted points), for $c = 0.4$ and $\phi = 4.5$eV, and their respective fraction of sites degraded (lines).

regimes occurs smoothly for $\rho(\gamma)$ Gaussian and exponential due the gradual degradation of the sites in the LAFE, as shown in Fig.6.3.

In the literature, the characteristic FEF of a LAFE, γ_C is communally associated to the "apparently FEF", $\beta^{FN} = -b\phi^{3/2}/S^{FN}$, where S^{FN} is the slope extracted from a ordinary FN plot. However, the possible existence of such linear behavior of the FN plot after the degradation of the LAFE has already started, show us one must be wary when it extracts information from the FN plot. This because the degradation of the LAFE initiates at the sites which more contribute to J_M. As consequence, S^{FN} decreases leading to high values of the β^{FN} which is associated to spurious values of γ_C. In order to show that, we calculate β^{FN} from the FN plot shown in Fig.6.4, which was simulated considering site FEFs exponentially distributed (see Fig.6.1) for $\delta = 0.4$ and $\phi = 4.5$eV, and compare its value with real γ_C after the end of the degradation process (i.e. at the minimum value of $1/F_M$). The results show that $\beta^{FN} \simeq 1815$ and $\gamma_C \simeq 421.87$, implying in a percentage relative difference of 430% between these two quantities. Thus, β^{FN} in these circumstances reflects spurious values of the real FEF of LAFE.

As completeness of our analyses, the orthodox test proposed by Forbes[126] was also performed. The results are presented in Fig.6.4. In order to do that, we estimate the effective (point by

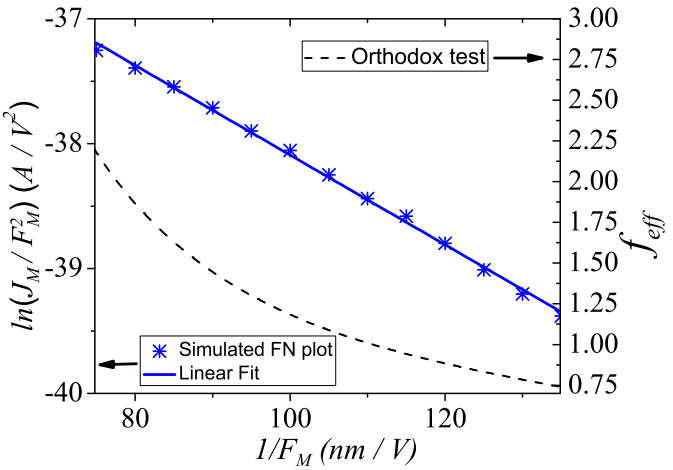

Figure 6.4: Fowler-Nordheim plot of a LAFE generated with FEFs exponentially distributed (see Fig.6.1), for $c = 0.4$ and $\phi = 4.5$eV. The (blue) full line is the linear fit, by least square procedure, to the simulated FN plot data (blue asterisks). The (black) dashed line is the estimation of the effective scaled barrier field, f_{eff} by using Eq.(6.4). Reasonable values for an orthodox emission predicts that f_{eff}, for $\phi = 4.5$eV, are expected to be in the range $0.10 \leq f_{eff} \leq 0.75$ [126].

point in ordinary FN plot) scaled field barrier f_{eff} as

$$f_{eff} = -\frac{s_t \eta}{S^{fit}\left(\frac{1}{F_M}\right)} \quad , \tag{6.4}$$

where s_t is the mathematical function that is the slope correction function for the SN barrier[116], $\eta = bc^2\phi^{-1/2}$, and $S^{fit} \equiv \frac{\partial(J_M/F_M^2)}{\partial(1/F_M)}$. In fact, the exact value of s_t is always unknown, but a good approximation for metals is 0.95, as used in this work. For $\phi = 4.5$eV the f-values for orthodox emission range $0.10 \leq f_{eff} \leq 0.75$[126]. Our results shown in Fig.6.4 clearly indicate that f_{eff} is fully outside of the reasonable range for orthodox emission. This result connects the lack of field emission orthodoxy with the mechanism of degradation in a LAFE.

Finally, as pointed out by Forbes [158], Ref. [31], which reported current-voltage characteristics from Au posts on flexible graphene film, has inconsistencies resulting in unexplained origin of the spurious values found for β^{FN}. As possibilities, Refs. [126] and [158] suggested that mutual-screening effect or field dependence in the array geometry should merit careful exploration. Interestingly, for post diameters of 100 and 200 nm, the corresponding extracted scaled barrier fields found by Forbes [158] were 1.5 and 2.3, respectively. Our results for f_{eff}, as shown in Fig. 6.4, are consistent with the these values and suggest a possible evidence that changing

in morphology of a LAFE with the increasing of the applied field is the main origin of the unorthodox emission results reported in Ref. [31].

6.4 Conclusions

In this work, we show that the degradation of a large area field emission may cause two relevant features over the corresponding FN plot: (i) saturation at high applied field regime and (ii) a nearly linear regime even after the degradation has been started. We attempt that a nearly linear FN plot can hide the degradation process resulting in a spurious estimation of the characteristic field enhancement factor of the LAFE, corroborated by the lack of orthodox emission. We also show that the transition from initial morphology to initialization of degradation behavior is reflected in the corresponding FN plot as a consequence of the initial distribution of FEFs, $\rho(\gamma)$, which indicates whether the LAFE is formed by either few or large number of emitting sites that contribute effectively for emission.

Chapter 7

Final Conclusions and Remarks

Throughout this thesis we use random Gaussian surfaces to study two distinct physical systems. By the physical statistical approach the Schramm-Loewner evolution has yielded to calculate exactly critical exponents and also gave insights into the probability distribution of the curves. Much of statistical systems are difficult to describe analytically, thus many conjectures have been done supported by numerical SLE tests. It is a very promising field which has shown to extend to new ones. Studying correlated processes might give interesting insights into some common Statistical Physics problems and lead to new results.

Firstly, in the chapter 2 by using the Fourier Filtering Method to generate a random surface, we investigated how two concrete examples of random surfaces and, in particular, the critical exponents are influenced by the presence of phase correlations and by changes in the distribution of the Fourier coefficient magnitudes and Fourier phases. We verified that long-range phase correlations in Fourier space lead to a translation of the random surfaces, and that they do not have any influence on their statistical properties. For different distributions of magnitude of Fourier coefficients our results suggest that there is no H dependence of the fractal dimension of the percolation cluster and susceptibility exponent. Although we did not find any influence over the critical exponents, from our knowledge, this was the first quantitative analyzes regarded to the distribution of the Fourier coefficient and phases.

It is not straightforward an analytical analysis of random processes. So, the numerical SLE

point of view has gained an increasing interest because, in the scaling limit, several systems like Loop-Erase random walk, Potts model, percolation, watersheds has shown to share SLE statistics. The connection between SLE and random surfaces is important, once several physical systems like Graphene, turbulence and grown surfaces may be represented by random surfaces.

In chapter 3 we showed numerically that curve from correlated random surfaces with $-1 \leq H \leq 0$, in the scaling limit, are consistent with SLE curves. Both numerically by, tests were performed, a direct SLE numerical test and the Markovian test (no time correlation of the driving function), has supported our conclusions. In the end, we also show the dependence between the fractal dimension of the curve and its respective κ.

After we have introduced the cold field electron emission theory for metals in the chapter 4 we proposed a more general criterion for detecting and interpreting nonorthodox field emission which can be applied to any distribution of local field enhancement factor in conducting large-area field emitter, in the chapter 5. Due to the consideration of the dependence of the emission area on applied field, as a byproduct of technological relevance, our results show that general effective scaled barrier field, f, values extracted from linear Fowler-Nordheim (FN) plots are outside of the "experimentally reasonable" range of values for physically orthodox emission. It is a very important result because just confirm what we have seen in several works with LAFEs. One must have clear that, an linear FN plot is a necessary but it is not a sufficient condition to characterize an orthodox emission.

In Chapter 6 we investigate the saturation of the FN plots. Much effort has been done to describe such behavior of the FN plot, which may be caused by different physical phenomena. In our LAFE, we have considered a possible degradation of random sites of the LAFE when their reached a threshold local electric field. Such degradation process is not rare to occur, just that one applies intense electric field on the emitter. We emphasize that a nearly linear regime on FN plot was identified even after the degradation has been started.

Finally, we conclude that, considering two physical phenomena as, emission area dependency on applied field and the degradation process, we still have identified a linear region on FN plot. Such conclusions corroborate what we have affirmed that it is not sufficient to extract a linear

FN plot from an experiment to guarantee that one follows the orthodox hypothesis. Compared with experiments on single emitters, experiments with LAFEs are quite new and therefore much have to be understood in order to describe and characterize correctly the emission process on LAFEs.

Much still it can be done in both themes. As examples, the numerical SLE test may provide insights regarded to universality classes of growth surfaces and even that be used in field emission phenomenon on LAFEs. Also, the complete characterization of LAFEs together with the correct interpretation of the FN plot is far to be completely understood due to the influence of several physical phenomena on FN plot. Therefore, as result of the technological importance of LAFEs this field is current and in progress construction.

Bibliography

[1] Gotsmann, B. & Lantz, M. A., *Nature Materials*, **12**, 59–65, (2012).

[2] de Assis, T. A., de Castro, C. P., de Brito Mota, F., de Castilho, C. M. C. & Andrade, R. F. S., *Phys. Rev. E*, **86**, 051607, (2012).

[3] Jiang, L., Zhao, X. & Wang, L., *PLOS ONE* **11**, e0153774, (2016).

[4] Bernard, D., Boffetta, G., Celani, A. & Falkovich, G., *Nature Physics* **2**, 124–128, (2006).

[5] Bernard, D., Boffetta, G., Celani, A. & Falkovich, G., *Phys. Rev. Lett.* **98**, 024501, (2007).

[6] Giordanelli, I., Posé, N., Mendoza, M. & Herrmann, H. J., *Scientific Reports* **6**, 22949 (2016).

[7] Nilsson, L., Groening, O., Groening, P., Kuettel, O. & Schlapbach, L., *J. of Appl. Phys.* **90**, 768 (2001).

[8] de Castro, C. P., de Assis, T. A., de Castilho, C. M. C. & Andrade, R. F. S., *J. of Phys.: Cond. Matter* **26**, 44 (2014).

[9] de Assis, T. A., Borondo, F., Benito, R. M. & Andrade, R. F. S., *Phys. Rev. B* **78**, 235427 (2008).

[10] de Assis, T. A., de Brito Mota, F., Miranda, J. G. V., Andrade, R. F. S. & de Castilho, C. M. C., *J. of Phys.: Cond. Matter* **19**, 47 (2007).

[11] Schramm, O., *Israel Journal of Mathematics* **118**, 221–288, (2000).

[12] de Castro, C. P., Lukovi, M., Andrade, R. F. S. & Herrmann, H. J., *Scientific Reports* **7**, 1961, (2017).

[13] Daryaei, E., Araújo, N. A. M., Schrenk, K. J., Rouhani, S. & Herrmann, H. J., *Phys. Rev. Lett.* **109**, 218701, (2012).

[14] Posé, N., Schrenk, K. J., Arajo, N. A. M. & Herrmann, H. J., *Scientific Reports* **4**, 5495, (2014).

[15] Lawler, G. F., Schramm, O. & Werner, W., *Mathematical research letters* **8**, 13-24, (2001).

[16] Forbes, R. G., Edgcombe, C. J. & Valdr, U., *Ultramicroscopy* **95**, 57 – 65 (2003).

[17] de Assis, T. A., Andrade, R. F. S., de Castilho, C. M. C., Losada, J. C., Benito, R. M. & Borondo, F., *J. of Appl. Phys.* **108**, 114512 (2010).

[18] de Assis, T. A., Benito, R. M., Losada, J. C., Andrade, R. F. S., Miranda, J. G. V., de Souza, N. C,, de Castilho, C. M. C., de Brito Mota, F. & Borondo, F., *J. of Phys.: Cond. Matter* **25**, 28 (2013).

[19] Forbes, R. G., *J. of Appl. Phys.* **120**, 054302 (2016).

[20] Harris, J. R., Jensen, K. L., Petillo, J. J., Maestas, S., Tang., W. & Shiffler, D. A., *J. of Appl. Phys.* **121**, 203303 (2017).

[21] Harris, J. R., Jensen, K. L. & Shiffler, D. A., *J. Phys. D.: Appl. Phys.* **48**, 385203 (2015).

[22] Dall'agnol, F. F. & de Assis, T. A., *J. Phys.: Condens. Matter* **29**, 40LT01 (2017).

[23] de Assis, T. A. & Dall'agnol, F. F., *Nanotechnology* **27**, 44LT01 (2016).

[24] de Assis, T. A. & Dall'agnol, F. F., *J. of Appl. Phys.* **121**, 014503 (2017).

[25] Jensen, K. L., Shiffler, D. A., Peckerar, M., Harris, J. R. & Petillo, J. J., *J. of Appl. Phys.* **122**, 064501 (2017).

[26] de Assis, T. A., *Scientific Reports* **5**, 10175 (2015).

[27] de Assis, T. A. & de Castro, C. P., *JVSTB* **35**, 052201 (2017).

[28] Forbes, R. G., Deane, J. H. B., Fischer, A. & Mousa, M. S., *Jordan J. of Phys.* **8**, 125 (2015).

[29] de Assis, T. A., *JVSTB* **33**, 052201 (2015).

[30] Forbes, R. G., *Nanotechnology* **23**, 095706 (2012).

[31] Arif, M.,Heo, K.,Lee, B. Y.,Lee, J.,Seo, D. H.,Seo, S.,Jian, J. & Hong, S., *Nanotechnology* **22**, 355709 (2011).

[32] Zhang, Z.,Meng, G.,Wu, Q.,Hu, Z.,Chen, J.,Xu, Q. & Zhou, F., *Scientific Reports* **4**, 4676 (2014).

[33] Kolosko, A. G.,Filippov, S. V.,Romanov, P. A.,Popov, E. O.,& Forbes, R. G., *JVSTB* **34**, 041802 (2016).

[34] Bonard, J. M., Kind, H., Stöckli & Nilsson, L. O., *Solid-State Electron.* **45**, 893 (2001).

[35] Bonard, J. M., k. A. Dean, Coll, B. F. & Klinke, C., *Phys. Rev. Lett.* **89**, 197602 (2002).

[36] Cole, M. T., Mann, M., Teo, B. K. & Milne, W. I., Emerging Nanotechnologies for Manufacturing, Micro and Nano Technologies. *2nd ed., edited by W. Ahmed and M. J. Jackson (William Andrew Publishing, Boston, 2015)* **pp. 125-186**.

[37] Devan, R. S., Ma, Y. R., More, M. A., Khare, R. T., Antad, V. V., PAtil, R. A., Thakare, V. P., Dhayal, R. S.& Schmidt-Mende, *RSC adv.* **6**,98722 (2012).

[38] Whaley, D. R., Gannon, B. M., Smith, C. R., Armstrong, C. M. & Spindt, C. A., *IEEE Trans. Plasma Sci.* **28**, 727 (2000).

[39] Basu, A., Swanwick, M. E., Fomani, A. A., & Velasquez–Garcia, *J. Phys. D: Appl. Phys.* **48**, 225501 (2015).

[40] Swanwick, M. E., Keathley, P. D., , Fallahi, A., Krogen, P. R., Laurent, G., Moses, J., Kärtner, F. X. & Velasquez–Garcia, *Nano Lett.* **14**, 5035 (2014).

[41] Wang, S., Calderon, X., , Peng, R., Schreiber, E. C., Zhou, O. & Chang, S., *Appl. Phys. Lett.* **98**, 213701 (2011).

[42] Kolosko, A. G., Popov, E. O., Filippov, S. V. & Romanov, P. A., 27th International Vacuum Nanoelectronics Conference (IVNC) (2014). **pp. 186–187**.

[43] Saberi, A. A., Niry, M. D., Fazeli, S. M., Rahimi Tabar, M. R. & Rouhani, S., *Phys. Rev. E* **77**, 051607 (2008).

[44] Kalda, J., *EPL (Europhysics Letters)* **84**, 46003 (2008).

[45] Olami, Z. & Zeitak, R., *Phys. Rev. Lett.* **76**, 247–250, (1996).

[46] Isichenko, M. B., *Reviews of Modern Physics* **64**, 961–1043, (1992).

[47] Schrenk, K. J. *et al.*, *Phys. Rev. E* **88**, 052102, (2013).

[48] Schmittbuhl, J., Vilotte, J.-P. & Roux, S., *J. Phys. A.* **26**, 6115–6133 (1993).

[49] Prakash, S., Havlin, S., Schwartz, M. & Stanley, H. E., *Phys. Rev. A* **46**, R1724–R1727, (1992).

[50] Weinrib, A., *Phys. Rev. B* **29**, 387–395, (1984).

[51] Mandelbrot, B., *The Fractal Geometry of Nature* (W. H. Freeman and Company, New York, 1982).

[52] Kondev, J. & Henley, C. L., *Phys. Rev. Lett.* **74**, 4580–4583, (1995).

[53] Boffetta, G., Celani, A., Dezzani, D. & Seminara, A., *Geophysical Research Letters* **35**, L03615, (2008).

[54] Barnsley, M. F. *et al.*, *The Science of Fractal Images* (Springer-Verlag, New York, 1988).

[55] Dietrich, S. & Amnon, A., *Introduction to Percolation Theory* (CRC PRESS, 1985).

[56] Kalda, J., *Phys. Rev. Lett.* **90**, 118501, (2003).

[57] Bauer, M. & Bernard, D., *Physics Reports* **432**, 115 – 221 (2006).

[58] Bernard, D., Le Doussal, P. & Middleton, A. A., *Phys. Rev. B* **76**, 020403, (2007).

[59] Fehr, E., Kadau, D., Araújo, N. A. M., Andrade, J. S. & Herrmann, H. J., *Phys. Rev. E* **84**, 036116, (2011).

[60] Amoruso, C., Hartmann, A. K., Hastings, M. B. & Moore, M. A., *Phys. Rev. Lett.* **97**, 267202, (2006).

[61] Schrenk, K. J., Araújo, N. A. M., Andrade Jr, J. S. & Herrmann, H. J., *Scientific Reports* **2**, (2012).

[62] Makse, H. A., Havlin, S., Schwartz, M. & Stanley, H. E., *Phys. Rev. E* **53**, 5445–5449, (1996).

[63] Lauritsen, K. B., Sahimi, M. & Herrmann, H. J., *Phys. Rev. E* **48**, 1272–1278, (1993).

[64] Oliveira, E. A., Schrenk, K. J., Araújo, N. A. M., Herrmann, H. J. & Andrade, J. S., *Phys. Rev. E* **83**, 046113, (2011).

[65] Ballesteros, H. G. & Parisi, G., *Phys. Rev. B* **60**, 12912–12917, (1999).

[66] Morais, P. A., Oliveira, E. A., Araújo, N. A. M., Herrmann, H. J. & Andrade, J. S., *Phys. Rev. E* **84**, 016102, (2011).

[67] Fehr, E., Kadau, D., Araújo, N. A. M., Andrade, J. S. & Herrmann, H. J., *Phys. Rev. E* **84**, 036116, (2011).

[68] MacDonald, D. K. C., *Noise and Fluctuations an Introduction* (Dover Plubications, Mineola, New York, 2006).

[69] Smirnov, S. & Werner, W., *Mathematical Research Letters* **8**, 729–744 (2001).

[70] Sandler, N., Maei, H. R. & Kondev, J., *Phys. Rev. B* **70**, 045309, (2004).

[71] Weinrib, A. & Halperin, B. I., *Phys. Rev. B* **27**, 413–427, (1983).

[72] Janke, W. & Weigel, M., *Phys. Rev. B* **69**, 144208, (2004).

[73] Schrenk, K. J., Araújo, N. A. M., Andrade Jr, J. S. & Herrmann, H. J., *Scientific Repeports* **2** (2012).

[74] Newman, M. E. J. & Ziff, R. M., *Phys. Rev. Lett.* **85**, 4104–4107, (2000).

[75] Newman, M. E. J. & Ziff, R. M., *Phys. Rev. E* **64**, 016706, (2001).

[76] Löwner, K., *Math Ann* **89**, 103, (1923).

[77] Smirnov, S., *C. R. Acad. Sci. Paris Sér. I Math* **333**, 239, (2001).

[78] Smirnov, S. & Werner, W., *Math Res. Lett.* **8**, 729, (2001).

[79] Henkel, M. & Karevski, D., Editors, *Springer* **83**, (2012).

[80] Gruzberg, I. A., *J. Phys. A : Math. Gen.* **39**, 12601–12655, (2006).

[81] Werner, W., *Ecole d'Et de Probabilits de Saint-Flour XXXII (2002)*, Springer Lecture Notes in Mathematics, **1180**, 113, (2004).

[82] Bauer, M. & Bernard, D., *Phys. Rep.* **432**, 115–221, (2006).

[83] Werner, W., An Introduction to Schramm-loewner Evolution and Related Topics. (2013).

[84] Cardy, J., *Phys. Rep.* **318**, 81-118, (2005).

[85] Kager, W. & Nienhuis, B., *J. of Stat. Phys.* **115**, 11491229, (2004).

[86] Lawler, G.F. & Sheffield, S., *The Annals of Probability* **39**, 8961937, (2011).

[87] Fong, C., Analytical Methods for Squaring the Disc. *arxiv/1509.06344* (2014).

[88] Belavin, A. A., Polyakov, A. M. & Zamolodchikov, A. B., *Nuclear Physics B* **241**, 333380, (1984).

[89] Majumdar, S. N., *Phys. Rev. Lett.* **68**, 2329-2331, (1992).

[90] Coniglio, A., *Phys. Rev. Lett.* **62**, 3054-3057, (1989).

[91] Smirnov, S., *Ann. Math.* **172**, 1435-1467, (2010).

[92] Schramm, O. & Sheffield, S., *Ann. Probab.* **33**, 2127-2148, (2005).

[93] Schramm, O. & Sheffield, S., *Acta. Math.* **202**, 21137, (2009).

[94] Schramm, O. & Sheffield, S., *Probab. Theory Relat. Fields* **157**, 4780, (2017).

[95] Rohde, S. & Schramm, O., *Selected Works of Oded Schramm* New York, NY: Springer New York, 2011, p. 989-1030.

[96] Beffara, V., *Ann. Probab.* **36**, 1421, (2008).

[97] Lawler, G. F., Schramm, O. & Werner, W., *Ann. Probab.* **32**, 939–995, (2004).

[98] Lawler, G. F., Schramm, O. & Werner, W., *Acta Mathematica* **187**, 237–273, (2001).

[99] Voss, R. F., *J. of Phys.s A: Mathematical and General* **17**, L373–L377 (1984).

[100] Sapoval, B., Rosso, M. & Gouyet, J., *J. de Phys. Lett.* **46**, 149–156, (1985).

[101] Lodhia, A., Sheffield, S., Sun, X. & Watson, S. S., Fractional Gaussian fields: a survey, arxiv/1407.5598, (2014).

[102] Smith Steven W., *The Scientist and Engineer's Guide to Digital Signal Processing.*

[103] Manna, S., *Physica A: Statistical Mechanics and its Applications* **391**, 2833–2841 (2012).

[104] Schrenk, K. J., Araújo, N. A. M. & Herrmann, H. J., *Phys. Rev. E* **87**, 032123, (2013).

[105] Kalda, J. *Phys. Rev. Lett.* **90**, 118501, (2003).

[106] Beffara, V. *Ann. Probab.* **36**, 1421, (2008).

[107] Saberi, A. A. *Phys. Rep.* **578**, 1-32, (2015).

[108] Kennedy, T. *J. Stat. Phys.* **131**, 803, (2008).

[109] Kennedy, T. *J. Stat. Phys.* **137**, 839, (2009).

[110] Kennedy, T. *J. Stat. Phys.* **128**, 1125–1137, (2007).

[111] Bauer, R. O., *Ann. Fac. Sci. Toulouse Math.* **12**, 432, (2003).

[112] Shi-Dong Liang, Quantum Tunneling and Field Electron Emission Theories, *World Scientific Publishing* **Singapore**, (2014).

[113] Ziman, J. M. Principles of the Theory of Solids, *Cambridge University* **Press: Cambridge**, (1964).

[114] Forbes, R. G., *Surf. Interface Anal.* **36**, 395 – 401 (2004).

[115] Sommerfeld, A. & Bethe, H. In Handbuch der physik, *vol. 24/2* Geiger H., Scheel K. (eds), **Springer:Berlin**, (1933).

[116] Forbes, R. G. & Deane, J. H., *Proceedings of the Royal society A* **463**, 2907–2927, (2007).

[117] Landau, L. D. & Lifschitz, E. M., Quantum Mechanics. *Oxford, UK*, **Pergamon**, (1958).

[118] Forbes, R. G., *JVSTB* **26**, 788 (2008).

[119] Deane, J. H. B. & Forbes, R. G., *J. Phys. A: Math. Theor.* **41**, 395301, (2008).

[120] Forbes, R. G., *Appl. of Phys. Lett.* **89**, 113122, (2006).

[121] Schottky, W., *Physik. Zeitschr* **15**, 872–878 (1914).

[122] Forbes, G. R., JVSTB. *17*, **534** (1999).

[123] Forbes, G. R., JVSTB. *17*, **526** (1999).

[124] Forbes, R. G. & Deane, J. H. B., *JVSTB* **28**, C2A33 (2010).

[125] Forbes, R. G., Deane, J. H. B., Hamid, N. & Sim, H. S., *JVSTB* **22**, 12222 (2004).

[126] Forbes, R. G., *Proceedings of the Royal Society A* **469** (2013).

[127] Forbes, R. G., Fischer, A. & Mousa, M. S., *JVSTB* **31**, 02B103 (2013).

[128] Qin, X., Wang, W. L.,Xu, N. S., Lia, Z. & Forbes, R. G., *Proceedings of the Royal Society A* **467**, 10291051 (2011).

[129] Forbes, R. G., *Appl. Phys. Lett.* **110**, 133109 (2017).

[130] Nilsson, L., Groening, O., Emmenegger, C., Kuettel, O., Schaller, E., Schlapbach, L., Kind, H., Bonard, J. M. & Kern, K., *Appl. Phys. Lett.* **76**, 2071 (2000).

[131] Nilsson, L., Groening, O., , Groening, P., Kuettel, O. & Schlapbach, L., *J. of Appl. Phys.* **90**, 768 (2001).

[132] Cole, M. T. *et al.*, *Scientific Reports* **4**, 4840 (2014).

[133] de Assis, T. A. & Forbes, R. G., *30th International Vacuum Nanoelectronics Conference (IVNC) (2017)*,pp. 228–229.

[134] Lauritsen, C. C., *Electron emission from metals in intense electric fields, Ph.D. thesis (California Institute of Technology, 1929)*.

[135] Zhu, N,, Xu, K., Zhai, Y., Di, Y., Zhang, Z., Chen, J., Cole, M. T., Milne, W. I. & Chen, J., *Funct. Nanostruct.* **2**,22 (2016).

[136] de Assis, T. A., Dall'Agnol, F. F. & Andrade, R. F. S., *J. Phys. D: Appl. Phys.* **49**, 344301 (2016).

[137] Forbes, R. G., *29th International Vacuum Nanoelectronics Conference (IVNC) - Technical Digest (2016)*,pp. 104.

[138] Hawley, R., *Vacuum* **10**, 310 (1960).

[139] Latham, R., *High Voltage Vacuum Insulation: Basic Concepts and Technological Practice (Elsevier Science, London, 1995)*.

[140] Han, J. W., Moon, D. I. & Meyyappan, M., *Nano Lett.* **17**, 2146 (2017).

[141] Popov, E. O., Kolosko, A. G., Filippov, S. V., & Terukov, E. I., *30th International Vacuum Nanoelectronics Conference (IVNC) (2017)*, pp. 280–281.

[142] Popov, E. O., Filippov, S. V., Kolosko, A. G., Romanov, P. A. & Forbes, R. G., *29th International Vacuum Nanoelectronics Conference (IVNC) (2016)*, pp. 1–2.

[143] Gröning, O., Küttel, O. M., Gröning, P. & Schlapbach, L., *JVSTB* **17**, 1970 (1999).

[144] Minoux, E. *et al.*, *Nano Lett.* **5**, 2135–2138 (2005).

[145] Bachmann, M. *et al.*, *JVSTB* **35**, 02C103 (2017).

[146] Li, S. Q., Liang, Y. X. & Wang, T. H., *Appl. Phys. Lett.* **88**, 053107 (2006).

[147] Lin, M.-C. & Liao, Y.-H., *JVSTB* **26**, 826 (2008).

[148] Xu, N. S., Chen, J., & Deng, S. Z., *Appl. Phys. Lett.* **76**, 2463 (2017).

[149] Nottingham, W. B., *Phys. Rev.* **49**, 78–97 (1936).

[150] Paulini, J., Klein, T. & Simon, G., *J. of Phys. D: Appl. Phys.* **26**, 1310 (1993).

[151] Dyke, W. P., Trolan, J. K., Martin, E. E. & Barbour, J. P., *Phys. Rev.* **91**, 1043–1054 (1953).

[152] Dyke, W. P. & Trolan, J. K., *Phys. Rev.* **89**, 799–808 (1953).

[153] Kyritsakis, A., Veske, M., Djurabekova, F. & Zadin, V., In *2017 30th International Vacuum Nanoelectronics Conference (IVNC)*, 38–39 (2017).

[154] Choi, Y. C. *et al.*, *Physica E: Low-dimensional Systems and Nanostructures* **86**, 52 – 57 (2017).

[155] Bonard, J. W., Maier, F., Stckli, T., Chtelain, A., de Heer, W. A., Salvetat, J. P. & Forr, L., *Ultramicroscopy* **73**, 7 (1998).

[156] Dean, K. A., Burgin, T. P. & Chalamala, B. R., *Apply. Phys. Lett.* **79**, 1873 (2001).

[157] Bonard, J. W., Klinke, C. Dean, K. A. & Coll, B. F., *Phys. Rev. B* **67**, 115406 (2003).

[158] Forbes, R. G., *Nanotechnology* **23**, 288001 (2012).

[159] Cahay, M. *et al.*, *Appl. Phys. Lett.* **105**, 173107 (2014).

[160] Cahay, M., Zhu, W., Peralulan, N., Fairchild, S. B., Forbes, R. G., Back, T. C. & Murray, P. T., *2016 29th International Vacuum Nanoelectronics Conference (IVNC) (2016)* pp. 1–2.

[161] Nordheim, L. W., *Proceedings of the Royal society A* **121**, 626–639 (1928).

[162] Cahay, M. *et al.*, *Appl. Phys. Lett.* **108**, 033110 (2016).

[163] Qin, X., Wang, W. & Lia, Z., *JVSTB* **29**, 031802 (2011).

[164] Fowler, R. H. & Nordheim, L., *Proceedings of the Royal Society A* **119**, 173–181 (1928).

[165] Forbes, R. G., *JVSTB* **17**, 526 (1999).

[166] Forbes, R. G., *J. Appl. Phys.* **120**, 054302 (2016).

[167] Murphy, E. L. & Good, E. H., *Phys. Rev.* **102**, 1464–1473 (1956).

[168] Rohde, S. & Schramm, O., *Ann. of Math.* **161**, 883 (2005).